Measurement and Modeling of Hydrogen Environment-Assisted Cracking in Monel K-500

RICHARD P. GANGLOFF, HUNG M. HA, JAMES T. BURNS, and JOHN R. SCULLY

Hydrogen environment-assisted cracking (HEAC) of Monel K-500 is quantified using slow-rising stress intensity loading with electrical potential monitoring of small crack propagation and elastoplastic *J*-integral analysis. For this loading, with concurrent crack tip plastic strain and H accumulation, aged Monel K-500 is susceptible to intergranular HEAC in NaCl solution when cathodically polarized at -800 mV_{SCE} (E_A, *vs* saturated calomel) and lower. Intergranular cracking is eliminated by reduced cathodic polarization more positive than -750 mV_{SCE}. Crack tip diffusible H concentration rises, from near 0 wppm at E_A of -765 mV_{SCE}, with increasing cathodic polarization. This behavior is quantified by thermal desorption spectroscopy and barnacle cell measurements of hydrogen solubility *vs* overpotential for planar electrodes, plus measured-local crevice potential, and pH scaled to the crack tip. Using crack tip H concentration, excellent agreement is demonstrated between measurements and decohesion-based model predictions of the E_A dependencies of threshold stress intensity and Stage II growth rate. A critical level of cathodic polarization must be exceeded for HEAC to occur in aged Monel K-500. The damaging-cathodic potential regime likely shifts more negative for quasi-static loading or increasing metallurgical resistance to HEAC.

DOI: 10.1007/s11661-014-2324-z

I. INTRODUCTION

MONEL K-500 (UNS N05500) is a precipitation hardened austenitic Ni-Cu-Al alloy that exhibits high strength, fracture toughness, and corrosion resistance in marine environments. However, this alloy is susceptible to environment-assisted cracking (EAC) when stressed in chloride solution with cathodic polarization. EAC was reported for threaded bolts in North Sea oil and gas platforms[1–9] and submarine components[10,11] where cathodic polarization protected steel coupled to Monel. Cracking in these environments was predominantly intergranular (IG) with limited transgranular (TG) morphologies reported.[12] Field cracking is not unexpected given the susceptibility of precipitation hardened Ni-based superalloys to IG and TG EAC.[13–16] However, the number of field failures is limited; and causal factors are not known among variations in Monel metallurgy, cathodic polarization, stress state, and interactions.

Literature establishes that hydrogen environment-assisted cracking (HEAC) is the likely mechanism for EAC in Monel K-500 in marine environments that include cathodic polarization. Nickel is susceptible to IG HEAC in electrolytes, particularly under cathodic polarization and in acidic solutions which promote atomic hydrogen (H) production,[16] as well as in low pressure H_2.[17] Precharged H caused IG internal-H-assisted cracking (IHAC) in Ni,[18,19] Ni-Cu solid solutions,[20] and Fe and Ni superalloys.[21,22] Ductile microvoid cracking in Monel K-500 transitioned to IG cracking due to precharged H followed by static loading in moist air [at 448 K to 533 K (175 °C to 260 °C)],[23] or by slow-rate rising displacement deformation in either air at 298 K (25 °C)[24] or NaCl solution with cathodic polarization.[25] The extent of IG IHAC increased with increasing concentration of precharged H,[24] consistent with well-known IHAC behavior of steels.[13] Low strength solid solution Monel Alloy 400 was susceptible to IG and TG IHAC.[26,27]

The severity of EAC in Monel K-500 in chloride solution increases with increasing cathodic polarization,[2,25,28] which increases the overpotential for H production from water reduction, thus increasing the amount of H.[29] Absorbed H migrates to the highly stressed-localized crack tip fracture process zone (FPZ) where damage nucleates.[13] HEAC in a precracked specimen is often dominated by H production and uptake on crack tip surfaces due to the short diffusion distance (~1 μm) to highly stressed FPZ damage sites.[13] However, long exposure time and reduced overpotential for H production at the crack tip[29] suggest that a bold-surface source of H must be considered for HEAC in Ni superalloys. A study of IN718 showed that the threshold stress intensity factor (K_{TH}) for HEAC in high pressure

RICHARD P. GANGLOFF and JOHN R. SCULLY, Professors, and JAMES T. BURNS, Research Assistant Professor, are with the Department of Materials Science and Engineering, Center for Electrochemical Science and Engineering, University of Virginia, Charlottesville, VA 22904. Contact e-mail: rpg7y@Virginia.edu. HUNG M. HA, formerly Research Scientist with the Department of Materials Science and Engineering, Center for Electrochemical Science and Engineering, University of Virginia, is now Post-Doctoral Research Fellow with the Department of Materials Engineering, University of British Columbia, Vancouver, BC V6T 1Z4, Canada.
Manuscript submitted July 16, 2013.
Article published online May 17, 2014

H_2 or acidified chloride decreased as a unique function of increasing concentration of H produced at the crack tip.[14] The HEAC crack path transitioned from slip band-based TG to IG with increasing H content.[14] Such a correlation has not been reported for Monel K-500 in aqueous chloride solution. Moreover, except for limited reports of apparent threshold properties,[28,30] fracture mechanics-based characterization of EAC is lacking for Monel K-500. Most studies used the slow strain rate method applied to a smooth- or blunt-notch specimen immersed in chloride solution to characterize EAC and isolate causal factors.[2–6,10,24,25,31,32] Metallurgical candidates include cold work prior to aging resulting in high hardness, alloy composition variation, grain boundary carbide/graphite, segregated impurities such as S, P or Se,[18] and grain boundary misorientation.[33] Investigation of the metallurgical factors which govern HEAC is outside the scope of the present study, but the approach reported here will inform such future work.

Proposed mechanisms for hydrogen cracking include: hydrogen-enhanced decohesion (HEDE), hydrogen-enhanced localized plasticity (HELP), and adsorption-induced dislocation emission (AIDE).[13,34] Others argue for cracking through or along a hydride ($(Ni,Cu)_xH$), which can form in Monel K-500 at 298 K (25 °C) and H contents of 10 to 25 parts-per-million by weight (wppm).[20,35–37] The contributions of these mechanisms to HEAC are controversial,[13,34] but recent transmission electron microscopy suggests interactive HEDE and HELP.[38] Boundary decohesion is enabled by local stress elevation from H-sensitive strain hardening, plus H enrichment due to slip band or substructure trapping of H and H transport from dislocation plasticity. Hydrogen also promotes increased slip band localization in the Ni matrix,[39] which could elevate micro-scale tensile stresses for IG decohesion (or favor TG slip band cracking). Electron microscopy did not evidence either hydride phase, cracking from such precipitates,[20] or super-abundant vacancy stabilization by H.[40]

It is critical to develop mechanism-based models, which predict quantitative HEAC kinetics for Monel K-500 in chloride solution, focusing on the effect of cathodic polarization and crack tip H concentration. The HEDE mechanism provides a basis for models which predict K_{TH}, as well as the upper-bound Stage II crack growth rate (da/dt_{II}) controlled by the rate limiting step in the production and FPZ diffusion of H.[13] The K_{TH} model developed by Gerberich *et al.*[41–43] successfully predicted the applied potential and H_2 pressure dependencies of K_{TH} in high strength steels:

$$K_{TH} = \frac{1}{\beta'} \exp \frac{(k_{IG} - \alpha C_{H\sigma})^2}{\alpha'' \sigma_{YS}}, \qquad [1]$$

where β' ($(MPa\sqrt{m})^{-1}$) and α'' (MPa m) are constants in a dislocation-shielding model of crack tip elastic stress, $C_{H\sigma}$ (atom fraction H) is the crack tip stress-enhanced diffusible H concentration adjacent to the crack path in the FPZ, and α (MPa$\sqrt{m}$ per atom fraction H) is a weighting factor which defines lowering of the Griffith toughness (k_{IG}, MPa$\sqrt{m}$) per unit H concentration. This model captures the interplay between crack tip plasticity and stress-based decohesion.[44]

For a wide range of high strength alloy-environment combinations that crack by HEAC, H diffusion in the crack tip FPZ limits da/dt_{II},[45] provided that surface reaction rate is rapid. Modeling of H diffusion ahead of a discontinuously propagating crack yielded[42,46]:

$$\left(\frac{da}{dt}\right)_{II} = \frac{4D_H}{x_{crit}} \left\{ \text{erf}^{-1}\left(1 - \frac{C_{H\sigma-crit}}{C_{H\sigma}}\right)\right\}^2, \qquad [2]$$

where D_H is the reversible-trap affected diffusivity of H, x_{crit} is the critical distance ahead of the crack tip where H cracking nucleates for a discontinuous crack advance increment, and $C_{H\sigma\text{-crit}}$ is the critical local concentration of H necessary for H cracking by decohesion at x_{crit}. $C_{H\sigma\text{-crit}}$ is a property of the interface and depends on local tensile stress *via* a failure criterion. $C_{H\sigma\text{-crit}}$ is related to the amount of local H ($C_{H\sigma}$) required to produce a local lowering of the intrinsic Griffith toughness, as qualitatively captured by the α term in Eq. [1].[22,46] x_{crit} reflects the interaction of crack tip tensile stress and H concentration gradient, and is of order 1 μm for high strength Ti, Fe, Al, and Ni-based alloys,[45] suggesting damage localization at the maximum in the crack tip σ_H distribution[47] or H-sensitive dislocation structure.[38,44] D_H for H in aged Monel K-500 at 298 K (25 °C) was reported to be 5 to 6×10^{-11} cm^2/s,[48] 1.5 to 1.9×10^{-10} cm^2/s,[24] and 9×10^{-11} to 4×10^{-10} cm^2/s,[29] suggesting an upper-bound da/dt_{II} from Eq. [2] of 20 to 160 nm/s. Equations [1] and [2] model cracking controlled by the interplay of crack tip stress and H to cause interface decohesion, independent of loading protocol. Lower levels of crack tip H uptake may increase the dependence of HEAC on plastic strain; the micromechanics must capture the loading format-history dependence of the crack tip strain field.[49]

$C_{H\sigma}$ in Eqs. [1] and [2] is in equilibrium with the crack tip overpotential for H production, and is derived as follows. Diffusible H concentration, $C_{H\text{-Diff}}$, is the sum of the lattice H concentration (C_L) and reversibly trapped H concentration (C_{RT}), assuming a single-reversible trap site with C_{RT} in local equilibrium with C_L and described using Fermi–Dirac statistics.[50] The lattice-interstitial H content is enhanced by the crack tip elastic stress field and a Fermi–Dirac distribution.[51] These considerations yield crack tip stress-enhanced $C_{H\text{-Diff}}$, which is $C_{H\sigma}$ in Eqs. [1] and [2]:

$$C_{H\sigma} = \left[C_L \frac{(1 - C_{L\sigma})}{(1 - C_L)} \exp\left(\frac{\sigma_H V_H}{RT}\right)\right] \left[1 + \frac{(1 - C_{RT})}{(1 - C_L)} \exp\left(\frac{E_B}{RT}\right)\right], \qquad [3]$$

where σ_H is crack tip hydrostatic stress given by 3 to 20 times alloy yield strength (σ_{YS}),[47] V_H is the partial molar volume of H in the Ni lattice (1.73 cm^3/mol H), E_B is the binding energy of H to the dominant-reversible trap site, $C_{L\sigma}$ is the concentration of stress-enhanced lattice H, and RT has the usual meaning. Equation [3] is based on the assumptions that σ_H increases C_L due to

lattice dilation,[51] thus enhancing C_{RT} in equilibrium with $C_{L\sigma}$, and that stress does not affect E_B. Equation [3] neglects H trapping at crack tip dislocation structure.[49,52,53] Research on H uptake and diffusion in Monel K-500,[29] extended in the present research, establishes the applied cathodic potential dependence of crack tip $C_{H\text{-}Diff}$ necessary to implement the models in Eqs. [1] through [3].[29] This approach was applied to model HEAC in ultra-high strength steels.[42,54]

The objectives of this research are to: (1) enhance an accelerated fracture mechanics test method for HEAC in moderate strength alloys,[42,55] (2) quantitatively characterize the HEAC kinetics of aged Monel K-500 in aqueous chloride solution with cathodic polarization, (3) establish $C_{H\sigma}$ *vs* applied cathodic potential for Monel K-500, and (4) model the applied potential dependencies of K_{TH} and da/dt_{II} based on crack tip H uptake using Eqs. [1] and [2]. Precracked specimens are loaded under slow-rising displacement, crack growth is monitored by a high precision direct current potential difference (dcPD) method, and the crack tip driving force is defined by an elastoplastic *J*-integral analysis which has not been broadly utilized to characterize HEAC.[56–58]

II. EXPERIMENTAL PROCEDURE

A. *Material and Specimen Design*

Hot finished and aged bar (15.9 mm diameter) of Monel K-500 was purchased from ATI Allvac with the vendor composition in Table I and mechanical properties in Table II. These properties were developed by hot working then age hardening: 16 hours at 866 K (593 °C), cool at 14 K/h (14 °C/h) to 755 K (482 °C), and air cool to ambient temperature. This heat treatment should result in coherent-spherical Ni_3Al precipitate strengthened (γ' phase of order 5 nm radius, 8 to 10 vol pct, and possibly with dissolved Ti, Cu, Si, or Mn) Ni-Cu solid solution austenite (face-centered cubic γ phase).[59] Ramberg–Osgood flow rule constants[60] were determined for this lot of aged Monel K-500 using compression loading to 2 pct total strain: $\alpha = 0.39$, $n = 20$, $E = 185{,}700$ MPa, and $\sigma_o = \sigma_{YS}$ (0.2 pct offset) = 786 MPa, consistent with Table II.

Single edge micronotch tensile (SENT) specimens were machined with a width (W) of 10.7 mm and thickness (B) of 2.54 mm.[42] The Mode I loading axis was parallel to the longitudinal direction (L) of the rod, with crack growth in the radial (R) direction. The notch was electrospark discharge machined to a depth of 200 ± 10 μm and mouth opening of 235 ± 20 μm. The SENT specimen was fatigue cracked in moist air to a notch plus short-crack depth (a_o) of 850 to 1150 μm, with the maximum-elastic stress intensity factor (K_{max}) decreasing from 18 to 13 MPa$\sqrt{m}$ at constant R (K_{min}/K_{max}) of 0.10.

B. *Crack Length Measurement*

The dcPD method was used to measure crack length with a constant direct current of 4.000 ± 0.005 A.[61] This procedure included current-polarity reversal to eliminate thermally induced voltages, crack potential difference normalization by a remote reference measurement, and active-normalized potential values averaged in groups of 50.[62] The resolution in measured potential was 0.1 μV, which corresponds to a resolvable average crack extension, Δa, of 0.5 μm. Each dcPD value was converted to crack length (a) by Johnson's calibration equation using the measured potential associated with the notch depth as the adjustable constant, V_o, in this equation.[63] All crack lengths from dcPD values were linearly corrected using the final optically measured crack length, which was averaged at five locations across the crack front. Predicted and measured crack lengths typically differed by less than 5 pct prior to linear correction.

To calculate crack growth rate (da/dt) at a given time (t), a 2nd order polynomial was fit to a–t data over 7 data points. The slope of the tangent at the mid-point was da/dt and this process was repeated to obtain da/dt at every a–t value. The da/dt was recorded for a crack advance increment, which exceeded 5 μm or for a time interval of 50,000 seconds if less than 5 μm of growth occurred. High resolution measurement of da/dt was challenged by two issues unique to this alloy strength and environment: (a) large scale ligament plasticity, which contributes to dcPD increase due to plasticity-based resistivity increase and tip blunting, and (b) crack surface electrical contact which decreases during crack opening. These issues resulted in a dcPD measurement resolution limit of da/dt between 0.2 and 1 nm/s for Monel K-500, as detailed in Section III.

C. *Fracture Mechanics Analysis*

Crack growth rate data were analyzed using elastic K and total stress intensity (K_J), which includes the effect

Table I. Chemical Composition of Monel K-500 (Weight Percent)

Ni	Cu	Fe	C	Mn	Al	Ti	P	S
66.12	28.57	0.80	0.166	0.81	2.89	0.45	0.015	0.0005

Si = 0.08; Cr = 0.04; Zr = 0.03; Nb, Ta, W, V < 0.01; Bi, Pb, Ag, Sn < 0.0005 wt pct.

Table II. Mechanical Properties of Monel K-500 (aged)

HRC	σ_{YS} (MPa)	σ_{UTS} (MPa)	Reduction in Area (pct)	E (GPa)	K_{IC} (MPa$\sqrt{m}$)
31	773	1169	49.7	183.9[102]	198 to 340[28,30,73]

of specimen plasticity from a J-integral analysis. Clevis gripping allowed free rotation of the SENT specimen to comply with the boundary condition for the elastic K solution using physical crack length, a.[64] K_J was determined using analytical solutions for a stationary crack in a material, which deforms according to the Ramberg–Osgood flow rule[60]:

$$K_J = \sqrt{(J_{Elastic} + J_{Plastic})E'} = \sqrt{\left(\frac{K^2}{E'} + J_{Plastic}\right)E'}, \quad [4]$$

where E′ is measured E for plane stress and $E/(1 - \nu^2)$ for plane strain and ν is Poisson's ratio. In Eq. [4] elastic K is based on effective crack length defined as physical crack length plus plane strain plastic zone correction[60]:

$$a_{eff} = a + \frac{1}{1 + \left(\frac{P}{P_o}\right)^2}\frac{1}{6\pi}\left(\frac{n-1}{n+1}\right)\left(\frac{K_{elastic}}{\sigma_o}\right)^2. \quad [5]$$

The plastic contribution to J in Eq. [4] is[65]:

$$J_{Plastic} = \frac{\alpha\sigma_o^2}{E}a\frac{(W-a)}{W}h_1(n, a/W)\left(\frac{P}{P_o}\right)^{n+1}, \quad [6]$$

where α, σ_o, and n are constants in the Ramberg–Osgood equation, E is σ_o/ϵ_o, a is crack length, W is SENT width, h_1 is a hardening and geometry dependent scaling function, P is load, and P_o is the limit load for net section plastic deformation given by[60]:

$$P_o = \beta\left(\sqrt{1 + \left(\frac{a}{W-a}\right)^2} - \left(\frac{a}{W-a}\right)\right)(W-a)B\sigma_o, \quad [7]$$

where B is thickness and β equals 1.455 for plane strain. The h_1 function for the rotating SENT specimen (n of 20) was defined by a sixth-order polynomial fit to discrete values and negative h_1 were precluded.[65] Stress state dependent terms in Eqs. [4] through [7] were assumed to be plane strain values, justified by three-dimensional finite element analyses[66,67] and the flat Mode I appearance of all EAC surfaces for Monel K-500.

D. *Electrochemical Control and Loading Conditions*

The precracked SENT specimen was loaded in a 340 mL cylindrical Plexiglas cell containing non-deaerated 0.6 M (3.5 wt pct) NaCl circulated from a 4 L reservoir at 20 mL/min and room temperature. Solution was not buffered and periodic measurements confirmed bulk pH of 6 to 7 for the duration of each experiment. Only the cracked section of the specimen was exposed to solution, precluding galvanic coupling with the grips. The SENT specimen (working electrode) was grounded through the test machine, while the potentiostat operated in floating mode to avoid a ground loop. Experiments were run in potentiostatic control with applied potential (E_A) from −1100 to −700 mV_{SCE}, compared to an open circuit potential of −200 to −250 mV_{SCE}[28] referenced to saturated calomel (SCE). The platinum-coated Nb-mesh counter electrode surrounded the specimen and the SCE was located in the cell. After immersion in NaCl solution, the specimen was cyclically loaded for 500 cycles at 1 Hz and the final precrack stress intensity range to assure that the aqueous environment contacted the crack tip.

The precracked SENT specimen was loaded under slow actuator displacement control in a servo-hydraulic machine. Displacement rate was varied in real time by computer control to provide a constant rate of elastic K increase, dK/dt, during crack growth. A loading protocol was programed to optimize test time: dK/dt = 5.5 MPa√m/h for elastic K up to 5.5 MPa√m where SCC is improbable, dK/dt = 0.33 MPa√m/h for K from 5.5 to 43.9 MPa√m, and dK/dt = 1.1 MPa√m/h for K above 43.9 MPa√m. These rates were selected based on experience with HEAC in steel[42] and IN718[14]; the effect of dK/dt was not measured for Monel K-500 in NaCl solution. A single test was performed in low humidity N_2 (<10 pct RH) at a dK/dt of 1 MPa√m/h.

E. *Occluded Crevice Electrochemistry and Local Hydrogen Concentration*

Modeling of HEAC using Eqs. [1] through [3] requires determination of a microstructure-specific H uptake relationship, stated as $C_{H\text{-}Diff}$ *vs* the overpotential for H production (η_H), coupled with knowledge of crack tip pH and potential to yield crack tip η_H; all *vs* E_A.[54] Crack-tip pH and potential were established for Monel K-500 using the artificial crevice geometry shown in Figure 1, coupled with the scaling-law approach to relate crevice and crack geometry difference.[68–70] The cell consisted of: (a) an acrylic bottom plate with six disk specimens embedded and shorted to form a continuous working electrode (WE), (b) a plastic shim to create the crevice gap (G), and (c) an acrylic top plate to form the crevice and hold micro-reference electrodes (REs) for local potential measurement. Monel K-500 specimens (surface area ~3 cm^2) were polished through 600 grit, degreased with ethanol, and mounted (Figure 1) at a distance (x) of 1, 3, 5, 7, and 9 cm from the crevice mouth to create x^2/G = 10, 90, 250, 490 and 810 cm. Only x was varied for fixed G of 1 mm. Crevice potential

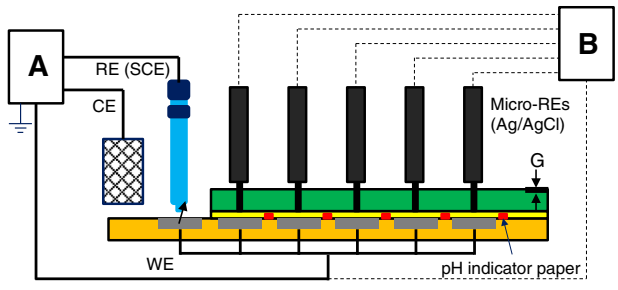

Fig. 1—(Color online) The artificial crevice electrochemical cell, where A is a potentiostat, CE is a counter electrode, and B is a multimeter to measure potential of 6-shorted alloy working electrodes (WE) in a crevice of opening-gap (G). Standard and micro-reference electrodes (RE) measured potential and indicator paper measured local pH.

was correlated with x^2/G because this parameter captures the geometric condition for equal-local potential in a crevice or crack.[54] Local potential was measured using a Ag/AgCl micro-reference electrode[54,71] calibrated *vs* a SCE. Local pH was measured using pH indicator paper. Electrolyte outside the crevice mouth was 0.6 M NaCl (pH = 6 to 7) and the cell was open to air.

The H uptake relationship for Monel K-500, $C_{\text{H-Diff}}$ *vs* E_A, was determined using either thermal desorption spectroscopy (TDS) or barnacle cell (BC) extraction of H using planar electrodes. Electrodes were H precharged for 10 days in 0.6 M NaOH maintained at pH 8 with NaOH addition. It is assumed that H uptake in the Monel K-500 crack is insensitive to local pH, at constant η_H for the expected pH levels above 6, as found elsewhere.[54] This data base was used to determine $C_{\text{H-Diff}}$ at each local potential for the value of x^2/G pertinent to crack opening shape in Monel K-500.

III. RESULTS

A. *Crack Tip Hydrogen Uptake*

Crack-tip pH and local potential, and associated H uptake, were established as a function of cathodic potential for Monel K-500.* Figure 2 shows local potential measured at different distances into the artificial crevice (x, for G = 1 mm) at external-E_A of −600 to −1000 mV_{SCE} for exposure in bulk 0.6 M NaCl at pH 6 to 7. In all cases a positive-potential gradient was established inside the crevice after external potential was applied. Local potential increased, due to IR drop and high current density, as x increased, and this potential gradient decreased with time due to decreased current density. No significant pH difference was observed as a function of x^2/G inside the crevice. However, pH increased with more cathodic E_A at 300 seconds exposure, and with increasing exposure time. Crevice pH measurements after 300 seconds exposure established this association: crevice pH 10 at E_A of −1000 mV_{SCE}, pH 8 at −900 mV_{SCE}, pH 8 at −800 mV_{SCE}, pH 7.5 at −700 mV_{SCE}, and pH 7 at −600 mV_{SCE}. The sharp change in crevice potential at 10 seconds (−900 mV_{SCE}) and at 5 hours (−1000 mV_{SCE}) are likely experimental anomalies.

The distribution of hydrogen overpotential inside the Monel K-500 artificial crevice was calculated from local pH and potential (Figure 2) for exposure in bulk 0.6 M NaCl at pH 6 to 7. Results are shown in Figure 3 as a function of E_A after 300 seconds and 10 hours exposures. At E_A of −600 and −700 mV_{SCE}, η_H was positive. At more negative-applied potentials (−800 and −900 mV_{SCE}), η_H was negative at 300 seconds but rose above 0 mV_{SCE} for longer time (10 hours). At −1000 mV_{SCE} and all time, η_H was always negative indicating net H production; overpotential was less negative with increasing distance from the crevice mouth and with time.

Total H content was measured for aged ATI Allvac Monel K-500 (Tables I and II) by both hot 923 K (650 °C) extraction and hot extraction-calibrated TDS, along with $C_{\text{H-diff}}$ from TDS and the BC methods, each *vs*

*It is assumed that crack tip potential and pH are not affected by heat-to-heat differences in Monel K-500. As such, a lot of Monel K-500 was investigated, which was used in a prior study[29]: Special Metals; Ni-30.2Cu-1.66Fe-0.17C-0.58Mn-2.69Al-0.61Ti-0.007P-<10 ppm S (by wt pct); aged at 866 K (593 °C) (16 hours), 811 K (538 °C) (6 hours), 755 K (482 °C) (8 hours), air cooled; σ_{YS} = 783 MPa, σ_{UTS} = 1146 MPa, and RA = 48 pct.

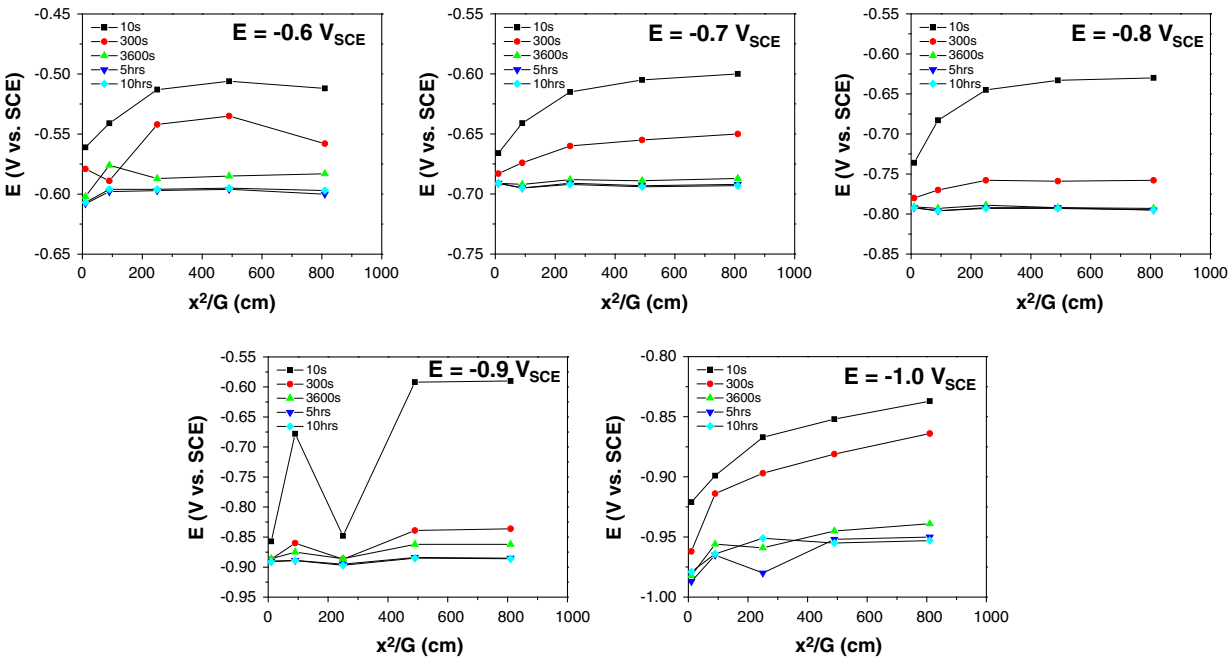

Fig. 2—(Color online) Local potential *vs* normalized position, x, along the artificial crevice with aged Monel K-500 (Special Metals lot, Footnote *), as a function of external-applied potential and exposure time in bulk 0.6 M NaCl solution. The crevice gap (G) was 1 mm.

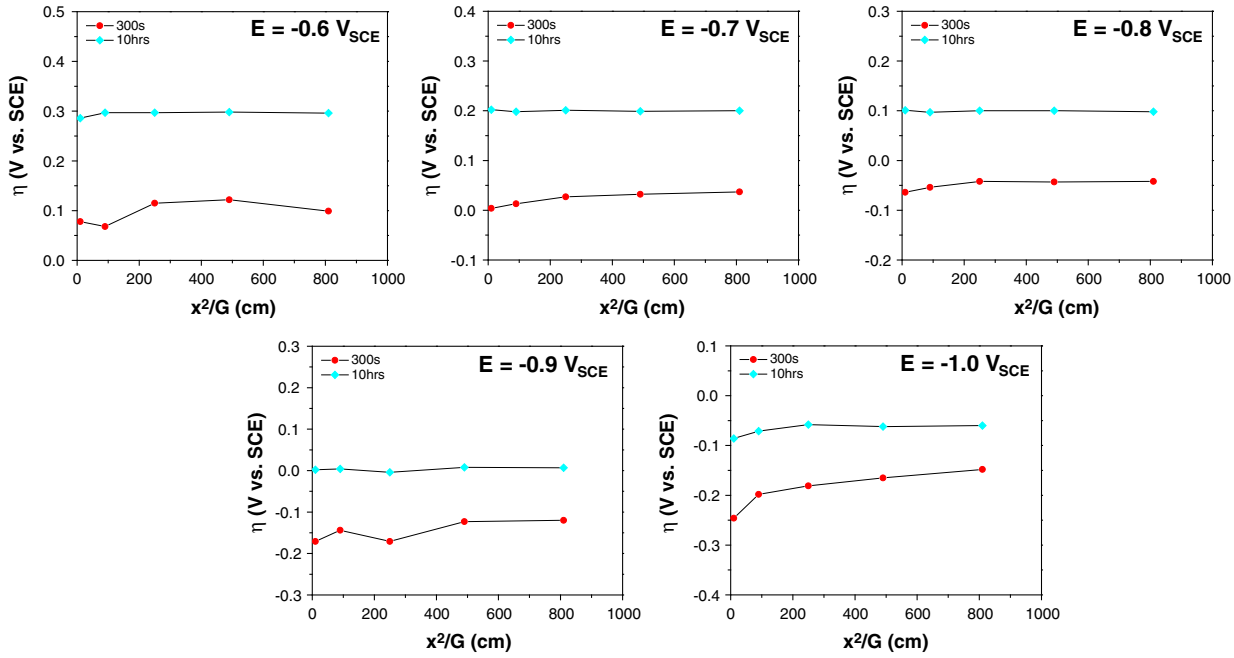

Fig. 3—(Color online) Local-H overpotential *vs* normalized distance into the artificial crevice with aged Monel K-500 (Special Metals, Footnote *), as a function of E_A for exposures of 300 s and 10 h in bulk 0.6 M NaCl, calculated using local potentials from Fig. 2. Solution pH at $x^2/G = 0$ was 6 at all times and applied potentials. After 300 s, pH values at all locations inside the crevice were 7, 7.5, 8, 8, and 10 when the E_A were −0.6, −0.7, −0.8, −0.9, and −1.0 V_{SCE}, respectively. After 10 h, pH at all locations inside the crevice was 11 at all E_A.

E_A for a boldly exposed planar coupon.[29] The results are shown in Figure 4, with the most reasonable H diffusivity for the BC data analysis being 1.3×10^{-10} cm^2/s for aged Monel K-500 at 298 K (25 °C).[29] The TDS and BC methods yielded different H uptake relationships, as also observed for a different lot of Monel K-500.[29] Regression through the TDS-based bold surface $C_{H\text{-}Diff}$ *vs* E_A data in Figure 4(□), converted to η_H for bulk NaOH solution pH 8, yielded:**

$$C_{H-Diff}(\text{wppm}) = -3.37 - 0.085\eta_H(\text{mV}). \quad [8]$$

The subsurface diffusible H concentration ($C_{H\text{-}Diff}$) at various x^2/G within the crevice was determined as a function of E_A using crevice-position dependent η_H (from measured-local potential and pH at 300 seconds immersion, Figure 3) coupled with the bold surface $C_{H\text{-}Diff}$ *vs* η_H relationship (Eq. [8]). Results are shown in Figure 5. Hydrogen uptake on the free surface ($x^2/G = 0$ cm) was computed using pH 6 in the calculation of η_H. The $C_{H\text{-}Diff}$ for this lot of aged Monel K-500 (ATI Allvac; Tables I and II), prior to H charging, was below the resolution of the TDS method.

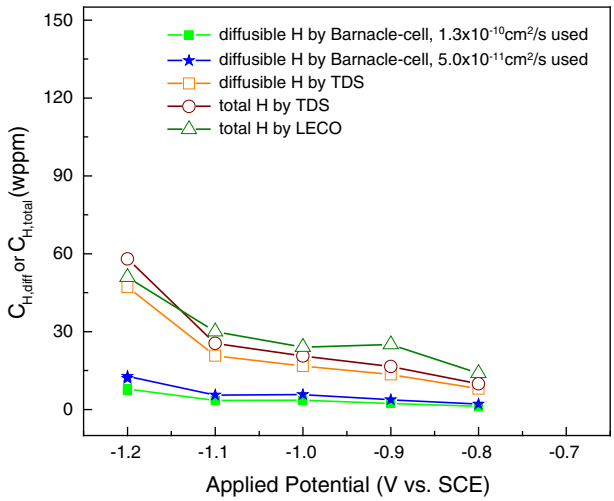

Fig. 4—(Color online) Dissolved total and diffusible H concentrations measured *vs* E_A for aged Monel K-500 (ATI Allvac, Table I) planar electrodes immersed in 0.6 M NaCl (pH 8 with NaOH addition). Barnacle Cell and hot extraction (LECO)-calibrated TDS methods were used, as detailed elsewhere.[29]

A typical SENT crack grows from 1.3 to 3.2 mm ($a = x$, including the 0.2 mm deep notch). The opening displacement (G in x^2/G) is approximated by the average of the elastoplastic crack tip opening displacement (CTOD) and elastic crack opening at the notch mouth.[60] This average opening varies from 14 to 33 μm for this crack extension interval at a typical K of 40 MPa$\sqrt{m}$. The associated x^2/G rises from 9 to 27 cm. For 1.3 mm < a < 3.2 mm, a twofold fall in K

**A similar trend was measured using hot extraction-calibrated TDS for the lot of aged Monel K-500 represented in Footnote *, and Figs. 2 and 3, and exposed in 0.6 M (pH 8) NaCl solution: $C_{H-Diff}(\text{wppm}) = -6.97 - 0.196\eta_H(\text{mV})$. The concentration of diffusible H was substantially higher in this lot of Monel K-500 compared to the ATI Allvac lot represented by Eq. [8].

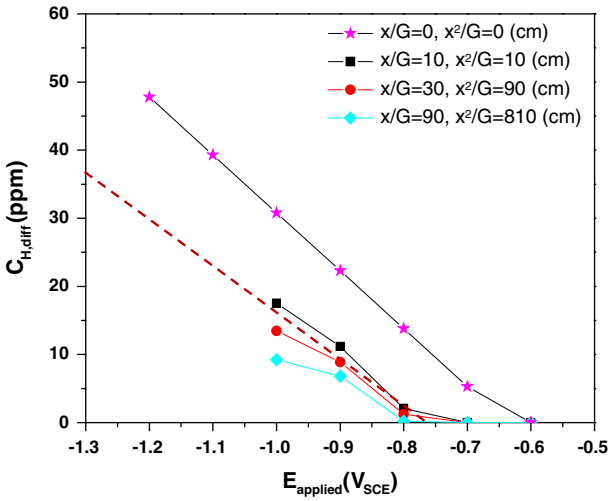

Fig. 5—(Color online) The effect of applied-external potential on diffusible H concentration produced at various locations within an artificial crevice for aged Monel K-500 (ATI Allvac, Table I), immersed in 0.6 M NaCl solution for 300 s. After 300 s, pH at $x^2/G = 0$ was 6 at all E_A; at all other locations, pH values were 7, 7.5, 8, 8, and 10 at applied potentials of −0.6, −0.7, −0.8, −0.9, and −1.0 V_{SCE}, respectively. $C_{H\text{-}Diff}$ is based on the TDS-established H uptake relationship in Fig. 4 and the dashed line is given by Eq. [9].

from 40 MPa√m results in $20 < x^2/G < 57$ cm, while a twofold rise in K from 40 MPa√m results in x^2/G of 12 cm for the 3.2 mm crack size typical of this high K of 80 MPa√m. Summarizing, x^2/G will be 10 to 60 cm for the range of crack sizes and K levels encountered in the crack growth experiments. The dotted line in Figure 5 describes crack tip $C_{H\text{-}Diff}$ *vs* applied potential for Monel K-500 (aged, ATI Allvac) SENT specimens with x^2/G of 10 to 60 cm; the equation is:

$$C_{H-Diff}(\text{wppm}) = -52.5 - 0.0687 E_A(\text{mV}_{SCE}). \quad [9]$$

Crack tip $C_{H,diff}$ decreases with increasing E_A. Equation [9] shows that H enters the crack tip at all applied cathodic polarizations more negative than −764 mV_{SCE}.

B. *Baseline Crack Growth in N_2*

The results of a slow-rising K experiment (dK/dt = 1 MPa√m/h) in low humidity N_2 (RH < 10 pct) are shown in Figure 6 and suggest two regimes of behavior. For $10 < K < 35$ MPa√m dcPD rises with K to produce da/dt on the order of 0.1 to 0.3 nm/s, which is not true crack advance. These false growth rates are due to crack tip plasticity, which causes increased alloy resistivity, and blunting. Highly localized plasticity is not corrected by remote-reference probe normalization. The data in this low-K regime are fit [log da/dt_{FALSE} (mm/s) = −6.96 + 0.01 K (MPa√m)] to establish a resolution limit. Similar-false da/dt behavior was observed for an ultra-high strength steel, which did not exhibit crack growth based on scanning electron microcopy (SEM).[72]

The second regime in Figure 6(a) shows da/dt rising above the resolution limit for K_J greater than 40 MPa√m. SEM analysis revealed a 700 μm wide zone of crack advance in the central portion of the SENT specimen (Figure 6(b)). This region is bounded by the fatigue precrack (right) and region where the applied load exceeded the limit load of the material (left). This extent of cracking during 45 hours of rising K from 40 to 85 MPa√m suggests an average da/dt of 4×10^{-6} mm/s. Higher resolution SEM analysis (Figure 6(c)) of the central region revealed features consistent with microvoid damage. The estimated upper bound of the stretch zone due to crack tip blunting equals CTOD and is ≈25 μm at K_J of 80 MPa√m[†]; this is small compared to the observed crack growth (700 μm).

[†]CTOD equals $d_n K_J^2(1 - \nu^2)/(\sigma_{YS} E)$[60], where $d_n = 0.69$ for the average of plane stress and plane strain, and using the Ramberg–Osgood flow properties for aged Monel K-500.

C. *HEAC under Severe Cathodic Polarization*

Aged Monel K-500 is susceptible to severe HEAC under slow-rising K during immersion in NaCl at constant-cathodic E_A of −1000 mV_{SCE}. Figure 7 shows the results of a single experiment, plotted as da/dt *vs* elastic K at constant dK/dt of 0.33 MPa√m/h for K from 6 to 43.9 MPa√m and dK/dt = 1.1 MPa√m/h for K above 43.9 MPa√m. A second experiment showed identical da/dt *vs* K, confirming reproducibility.[55] The initial decline in da/dt with rising K is not real; rather, it is due to crack surface electrical contact, which declines with rising K. Increasing voltage, at a declining rate with crack opening, is reasonable for Monel K-500 in NaCl because: (a) cathodic polarization likely reduced the fatigue crack surface oxide that would provide electrical insulation, and (b) the fatigue crack was microscopically rough due to slip band cracking to promote asperity contact (top part of Figure 8(a)). Falling log da/dt was fit as a linear function of log K and subtracted from measured da/dt to produce real growth rates. Correction of measured da/dt (filled data points in Figure 7) is illustrated by the solid line and open points. The corrected da/dt *vs* K relationship in Figure 7 conforms to the kinetics typical of HEAC.[13] An apparent K_{TH} for the onset of subcritical crack growth under slow-rising K is followed by steeply rising da/dt, and transitioning to the beginning of a reasonably K-independent (Stage II) crack growth rate regime above about 4×10^{-5} mm/s. The programmed increase of dK/dt at K = 44 MPa√m did not resolvably affect da/dt. The K_{TH}, operationally defined in a subsequent section, is 22 MPa√m in Figures 7 and 17 MPa√m for the replicate experiment. These K_{TH} are low compared to the plane strain fracture toughness for this alloy in the range of 198 to 340 MPa√m.[28,30,73]

The HEAC path was IG for the test conditions in Figure 7, as established by the SEM fractographs in Figure 8. The low magnification image (Figure 8(a)) shows the moist air fatigue precrack front transition to IG HEAC. Air fatigue in this alloy stressed at low stress intensities involves faceted {111} slip band cracking, plus limited IG cracking.[74] The transition from fatigue crack

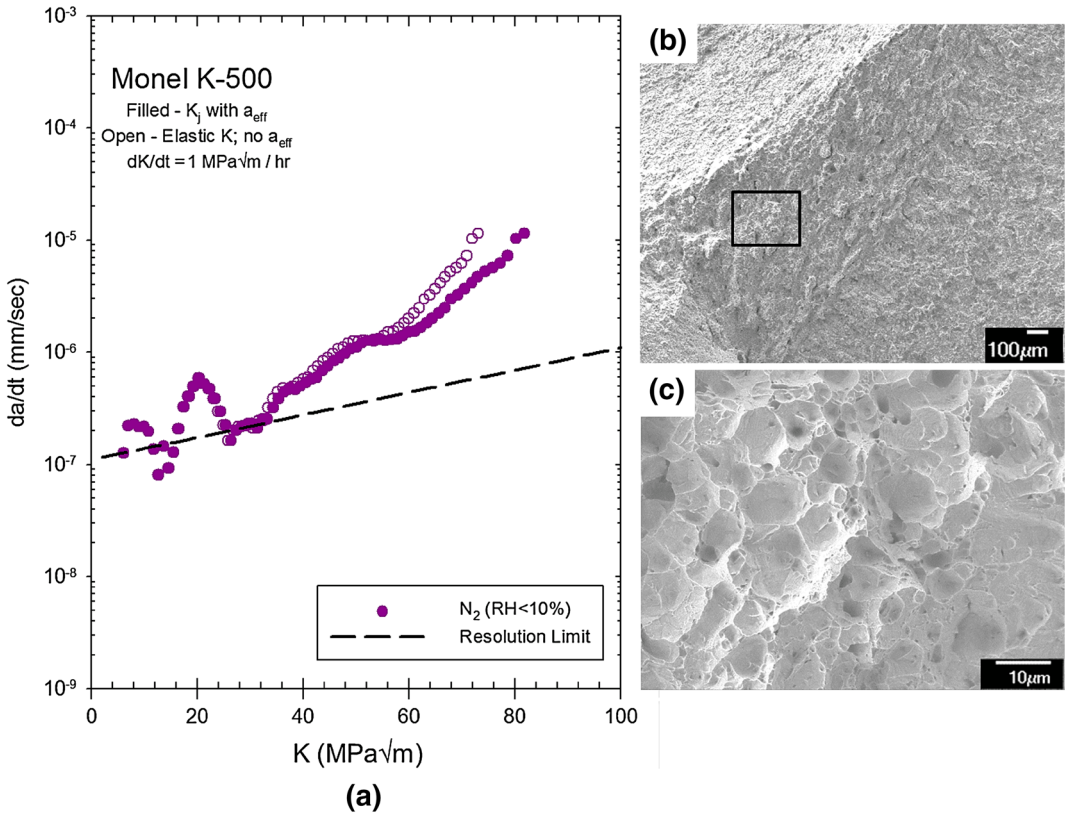

Fig. 6—(Color online) (*a*) Crack growth rate *vs K* (elastic, open and elastic–plastic, filled) for aged Monel K-500 (ATI Allvac, Table I) stressed at constant d*K*/d*t* of 1 MPa√m/h in low humidity N_2. The dotted line shows the resolution limit corresponding to false d*a*/d*t* from crack tip plastic deformation. SEM fractographs in (*b*) and (*c*) demonstrate crack growth (right to left) of a ductile morphology.

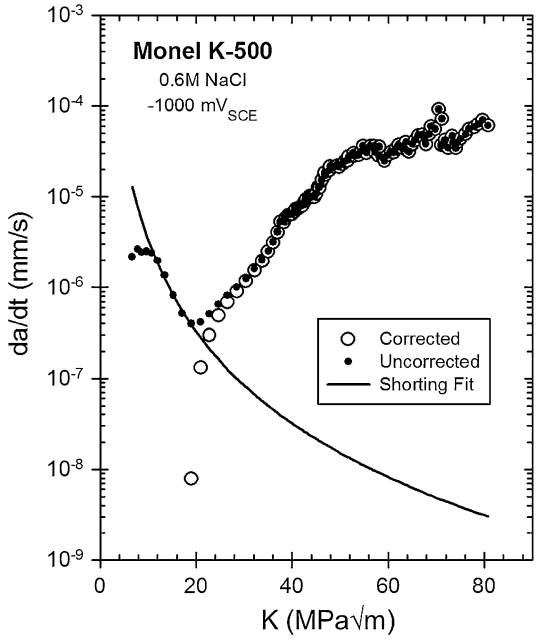

Fig. 7—Measured d*a*/d*t vs* elastic *K* for aged Monel K-500 (ATI Allvac, Table I) stressed under the slow-rising *K* protocol in NaCl solution at E_A of −1000 mV_{SCE}.

to H crack is traced in Figure 8(a) and was observed during SEM analyses of all specimens. This low magnification fractograph is compared to an SEM image (Figure 8(b)) of the Monel K-500 microstructure showing good correspondence between grain size and IG facet size. Figures 8(c) and (d) suggest that grain surfaces are populated by slip steps, which interact with grain boundaries as reported for IHAC of Ni.[38,39] The particles in Figure 8(b) are large TiC and sulfide inclusions (rich in Mg, Mn, Al, Ti, and Fe based on energy dispersive analysis)[29] and were occasionally present on IG surfaces. The fine particles in Figure 8(d) were not identified, but were observed on IG facets produced at other cathodic potentials. These particles are sized (~50 nm diameter) on the scale of Ni_3(Al,Ti) precipitates.[59]

D. *Effect of Applied Potential on HEAC*

The severity of HEAC in aged Monel K-500 increases with increasing cathodic polarization between −700 and −1100 mV_{SCE}, as established in Figure 9. Polarization current was nearly constant at each fixed E_A and always cathodic. K_{TH} is defined as the stress intensity level necessary to produce a d*a*/d*t* equal to the resolution limit represented by the dotted lines in Figure 9.‡

‡The levels of crack tip plasticity and false dcPD rise are expected to be independent of loading rate. As such, the false growth rate for d*K*/d*t* = 1 MPa√m/h (Fig. 6: log da/dt_{FALSE} (mm/s) = −6.96 + 0.01 K (MPa√m)) scales linearly with d*K*/d*t* to yield the loading rate specific resolution limit on d*a*/d*t*.

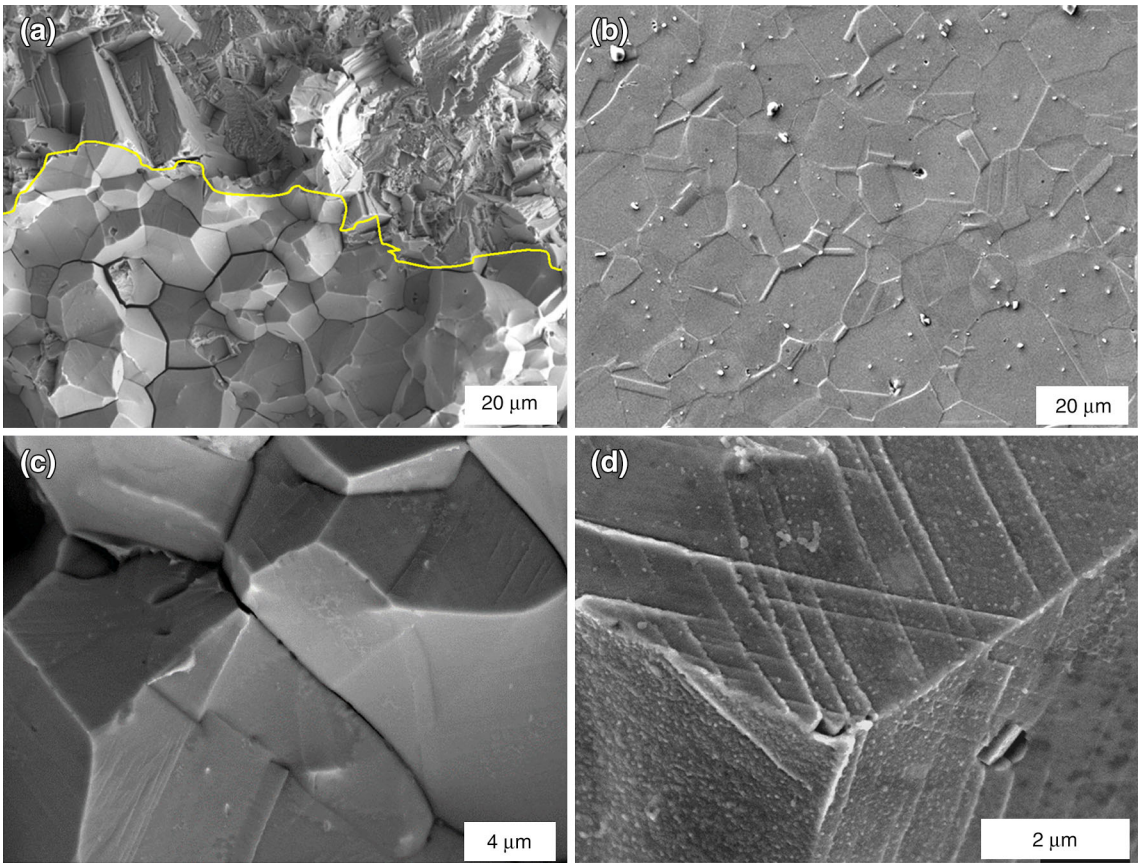

Fig. 8—(Color online) (*a*), (*c*), (*d*) Scanning electron fractographs for aged Monel K-500 (ATI Allvac, Table I), stressed under dK/dt of 0.3 MPa$\sqrt{m}$/h in NaCl solution at E_A of −1000 mV_{SCE}, showing IG HEAC transitioning from the mixed TG–IG fatigue crack front outlined in (a). Crack growth is from top to bottom in each image. (*b*): Scanning electron micrograph of polished and etched Monel K-500.

Table III summarizes these K_{TH} values, as well as data obtained for a second lot of aged Monel K-500 defined in Footnote *. All cracks grew in a flat Mode I morphology, with the exception of two experiments at −850 mV_{SCE}, which deflected out-of-plane after the onset of growth at K_{TH}. As such, the listed da/dt values may not be accurate and these two experiments are not included in Figure 9.

Three trends are apparent in Figure 9 and Table III. First, K_{TH} increases as E_A becomes more positive from −1100 to −700 mV_{SCE}. Second, crack growth rates approaching a Stage II plateau decrease with increasing potential. Third, the step increase in dK/dt (from 0.33 to 1.1 MPa$\sqrt{m}$/h) at K of 44 MPa$\sqrt{m}$ had no resolvable effect on da/dt at −1100 mV_{SCE}, but caused a step increase in da/dt at −800, −750, and −700 mV_{SCE}. For these higher potentials, Figure 9 shows an instantaneous 3.3-times increase in da/dt at K = 43.9 MPa$\sqrt{m}$, which equals the 3.3-times increase in applied dK/dt.

For E_A between −1100 and −900 mV_{SCE}, HEAC in Monel K-500 was macroscopically uniform through the SENT thickness and fully IG based on SEM analysis (*e.g.*, Figure 8). However, fractographic analysis of the −800 mV_{SCE} case (Figure 10) showed a mixed IG and TG morphology. The TG features suggest H interaction with slip to produce facets possibly parallel to intersecting slip planes. This TG cracking may be related to the lower H content produced at the crack tip for this higher potential, consistent with da/dt levels that decrease with increasingly positive E_A (Figure 9; Table III). SEM fractography of the −700 mV_{SCE} (Figures 11(a) and (b)) and −750 mV_{SCE} (Figures 11(c) and (d)) specimens did not evidence IG cracking. Rather, the crack surfaces produced in NaCl exhibited TG features similar to those observed for the low humidity N_2 experiment. Crack extension occurred in the central portion of each SENT specimen and was populated by microvoid features. The fractograph of the −700 mV_{SCE} specimen in Figure 11(a) shows the fatigue precrack in the top-third of the image, a 75 μm-wide-zone (middle) associated with slow-rising K loading in NaCl, and post-test fatigue in moist air (bottom third). The middle zone created by cracking in NaCl consists of dimple-like features without IG facets (Figure 11(b)). For the −750 mV_{SCE} case, Figure 11(c) shows a larger TG zone (~450 μm) in the central portion of the specimen, created during loading in NaCl and flanked by the fatigue precrack (left) and post-test fatigue (right). This middle zone is TG-dimpled, without evidence of IG features (Figure 11(d)).

E. *Effect of Loading Protocol on HEAC*

Loading protocol appears to significantly impact crack growth in aged Monel K-500, predominantly at

the less-cathodic potentials where resistance to HEAC is high. This behavior was examined at −800 mV_{SCE} by comparing crack growth during continuously slow-rising K (Figures 9 and 10) with a set of fast-rising step (1.5 MPa√m step at dK/dt = 7 MPa√m/h) then constant K hold (6 hours) segments. The SEM images in Figure 12 are striking. Figure 12(a) shows that 580 μm of uniform IG EAC (Figure 10) occurred during slow-rising K from an elastic K_{TH} of 42 MPa√m to a final-elastic K of 59.2 MPa√m (Figure 9) over 132.3 hours. A smaller amount of stable crack growth was observed for the step-hold case, with a final-elastic K of 53.5 MPa√m and total loading time of 120.7 hours. Critically, the crack path was TG with microvoids in the center of the SENT specimen (Figure 12(b)). This morphology is similar to that shown in Figures 6 and 11 for rising K loading in N_2, as well as in NaCl at −700 and −750 mV_{SCE} where HEAC did not occur.

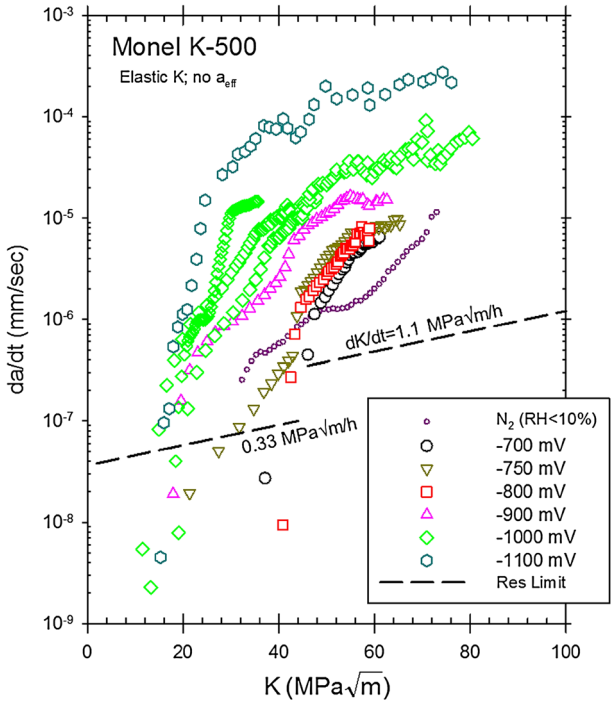

Fig. 9—(Color online) Crack growth rate *vs* elastic K for aged Monel K-500 (ATI Allvac; Table I) stressed under the slow dK/dt protocol in NaCl solution at various constant E_A between −700 and −1100 mV_{SCE}. Constant dK/dt was 0.33 MPa√m/h for $K < 43.9$ MPa√m and 1.1 MPa√m/h for $K > 43.9$ MPa√m. The dotted lines show the expected false da/dt produced by crack tip plastic deformation for each dK/dt.

Crack length during several hold periods is presented in Figure 13. From regression analysis, da/dt values are 5.6×10^{-8}, 1.3×10^{-8}, and 1.4×10^{-7} mm/s for K of 50.3, 51.9, and 53.5 MPa√m, respectively. These growth rates are associated with the real-stable crack growth indicated in Figure 12(b). The step increases in crack length were caused by crack tip deformation-based dcPD increase (false growth) plus real microvoid-based crack growth. Total crack growth was 276 μm from dcPD, overestimated due to crack tip plasticity and in reasonable agreement with the largest crack length change (250 μm) shown in Figure 12(b). These rates of crack growth are at least 30 times less than the da/dt characteristic of IGSCC at this E_A and slow-rising K, 4×10^{-6} mm/s at 53.5 MPa√m from Figure 9. Moreover, each of these hold-period K levels is above the K_{TH} for slow-rising loading. The results in Figures 12 and 13 suggest that step-hold K loading does not produce any IG EAC, which was created during slow-rising K loading, but did produce limited ductile crack growth as observed for other loading and environmental conditions. Experiments at higher K levels are required to examine this loading protocol effect.

Both slow rising and step-hold stress intensity protocols yielded the same rates of HEAC in aged Monel K-500 (Footnote *) when the specimens were stressed at −934 mV_{SCE}, which favored higher rates of subcritical cracking.

F. *Elastoplastic Analysis*

Neither macroscopic through-thickness plasticity, nor shear walls along specimen edges were associated with the HEAC results in Figure 9. Nonetheless, the high-elastic K achieved near the end of the experiments and relatively low strength of Monel K-500 necessitate

Table III. HEAC Growth Rate Properties for Aged Monel K-500 (ATI Allvac; Tables I and II)

E_A (mV_{SCE})	K_{TH} (elastic) (MPa√m)	K_{TH} (*J*-integral) (MPa√m)	da/dt_{II} from dcPD at elastic K = 50 MPa√m (mm/s)	IG cracking
−1100	17	17	1.7×10^{-4}	yes
−1000	20	20	2.3×10^{-5}	yes
−1000	16	16	1.9×10^{-5}	yes
−1000	18	18	1.8×10^{-5}	yes
−934 Footnote *	~30	~31	1.6×10^{-5}	yes
−900	19	19	1.1×10^{-5}	yes
−850	38	39	3.7×10^{-6} deflected	not examined
−850	41	44	2.5×10^{-6} deflected	not examined
−800	42	45	3.0×10^{-6}	yes
−750	>68	>90	N/A	no
−700	>63	>77	N/A	no
−700 Footnote *	>63	>77	N/A	no

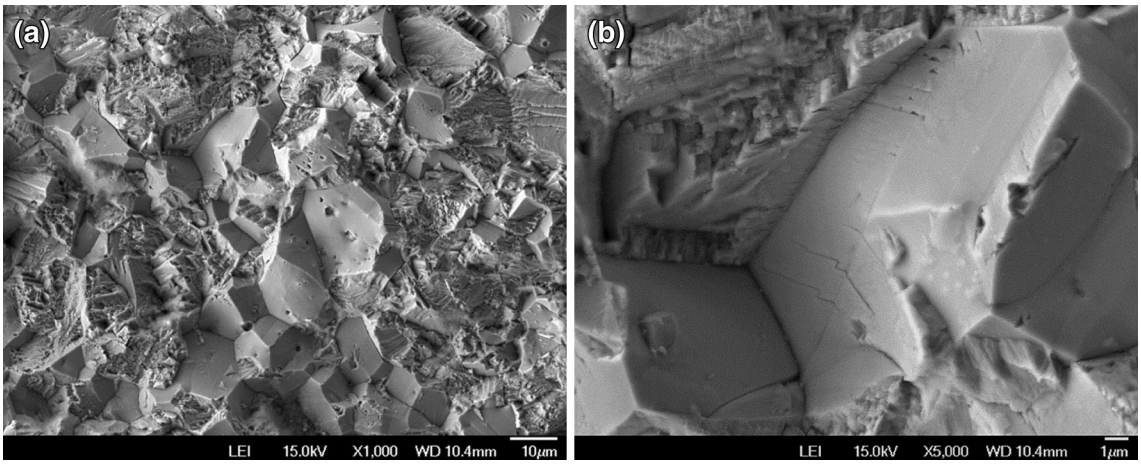

Fig. 10—Scanning electron fractographs of aged Monel K-500 (ATI Allvac; Table I), stressed under slow-rising K in NaCl solution at E_A of -800 mV_{SCE}, showing mixed IG–TG HEAC without microvoids.

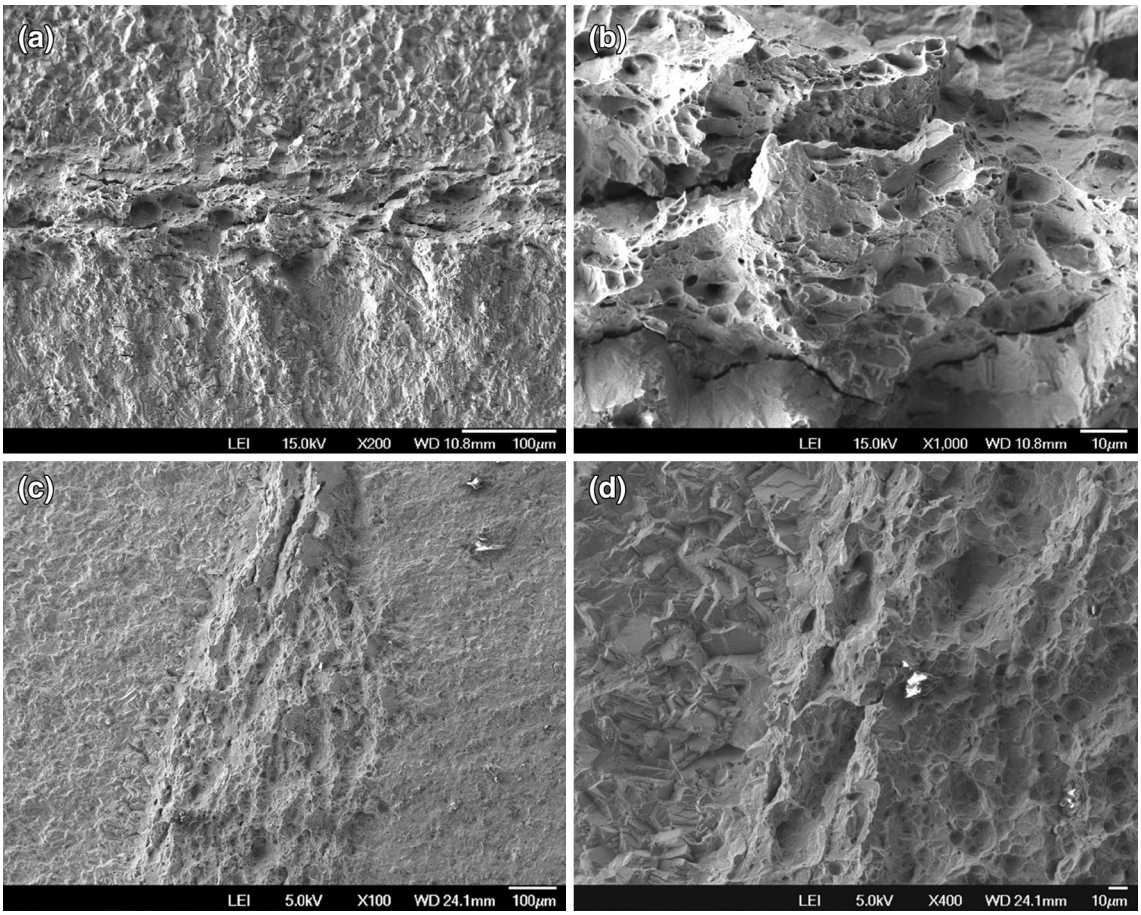

Fig. 11—Scanning electron fractographs of aged Monel K-500 (ATI Allvac; Table I) stressed under the slow-rising K protocol in NaCl at E_A of: (*a*) and (*b*) -700 mV_{SCE}, showing a lack of resolvable IG HEAC ahead of the fatigue crack front (middle of each image) with growth from top to bottom; and (*c*) and (*d*) -750 mV_{SCE}, showing a lack of IG cracking ahead of the fatigue crack (middle of each image) with growth from left to right.

assessment of the effect of uncracked ligament plasticity on stress intensity. Results are presented in Figure 14, which is a plot of da/dt *vs* elastic K (open symbols, plotted from Figure 9), and elastoplastic K_J (filled symbols) from the J-integral analysis of the SENT geometry. These results demonstrate no impact of plasticity for elastic K below about 40 MPa$\sqrt{m}$. However, elastoplastic analysis yields up to a 25 pct increase

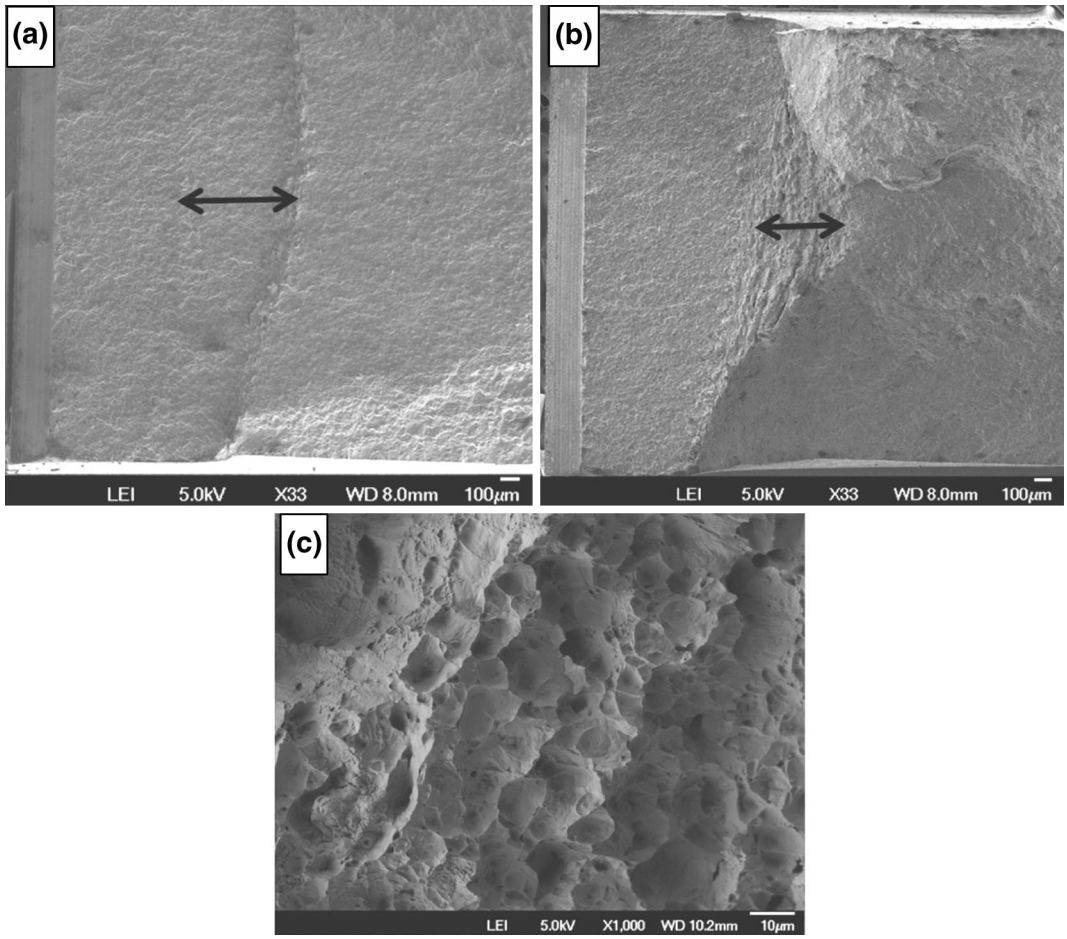

Fig. 12—SEM fractographs showing the effect of: (*a*) continuous-rising K (dK/dt = 0.33 MPa√m/h then 1.1 MPa√m/h) *vs* (*b*) and (*c*) step-hold K (2.6 MPa√m step at 7 MPa√m/h and 6 h hold; repeated) for aged Monel K-500 (ATI Allvac; Table I) stressed in NaCl solution at −800 mV_{SCE}.

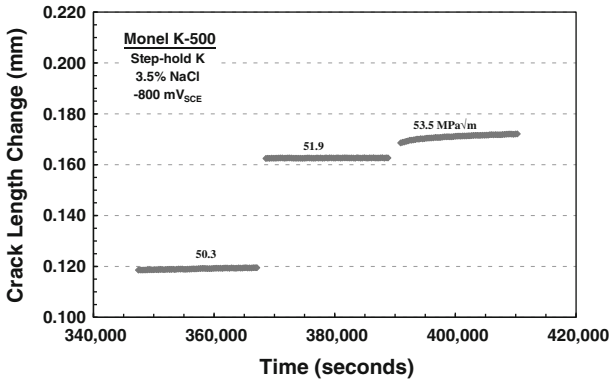

Fig. 13—Crack length change ahead of the fatigue precrack *vs* loading time for aged Monel K-500 (ATI Allvac; Table I) stressed under the fast-rise plus hold protocol at the indicated-constant elastic K levels during exposure in NaCl solution at −800 mV_{SCE}. Average da/dt from regression analysis of each data set is 5.6×10^{-8}, 1.3×10^{-8}, and 1.4×10^{-7} mm/s for the low to high K levels, respectively.

in K to K_J, with the strongest influence on experiments conducted with cathodic polarization above −800 mV_{SCE}. K_{TH} values are only mildly increased (Table III) and the estimated levels of da/dt_{II} are unaffected by this plasticity correction.

IV. DISCUSSION

A. *Accelerated-Quantitative Laboratory Characterization of EAC in Monel K-500*

The rising K small crack test method successfully characterized IG EAC in aged Monel K-500, providing quantitative K_{TH} and da/dt *vs* K data (Figures 9 and 14). Continuously recorded high resolution crack length measurement by dcPD, and the potentially damaging role of concurrent straining and H uptake, provides the basis for this accelerated test method. The steps necessary to obtain high resolution measurements of low growth rates were summarized in Section III and elsewhere.[72]

If an alloy is susceptible to HEAC, such as Monel K-500 under severe cathodic polarization in chloride solution, then cracking kinetics are similar for rising K and quasi-static K or step-hold loading; dcPD monitoring of the small crack to yield K_{TH} and da/dt *vs* K is the primary attribute of this method. Measurement of da/dt

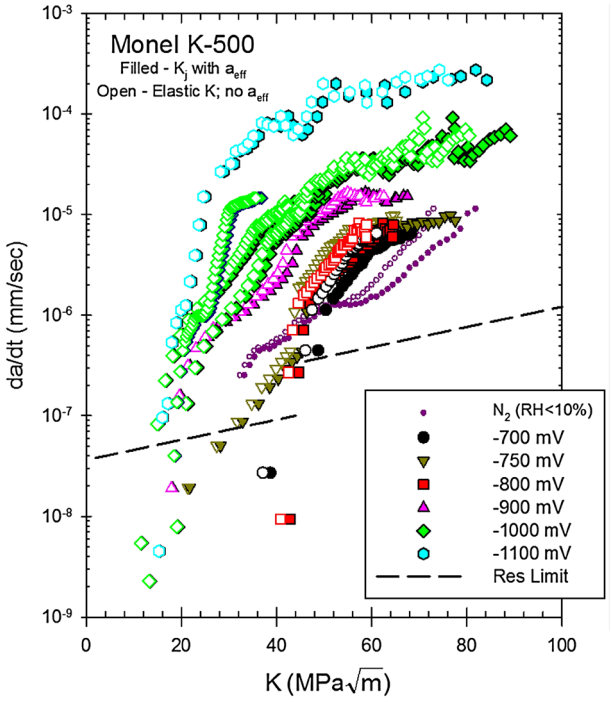

Fig. 14—(Color online) da/dt *vs* K for aged Monel K-500 (ATI Allvac; Table I) stressed under slow-rising K in NaCl solution at various constant E_A between −700 and −1100 mV_{SCE}. da/dt is plotted *vs* elastic K (open) from Fig. 9 and elastic–plastic K_J (filled). The constant dK/dt was 0.33 MPa√m/h for $K < 43.9$ MPa√m, then 1.1 MPa√m/h for higher K. The dotted lines show estimated-false da/dt produced by crack tip plastic deformation for each dK/dt.

over short-crack extension and time (days to weeks) provides the basis to predict cracking over longer times in alternate geometries, following fracture mechanics similitude.[72] The rapid rise in da/dt above the apparent K_{TH} enables such long-term predictions. However, for alloys which resist environmental cracking leading to a strong role of crack tip plasticity in HEAC,[49] or if crack tip surface condition or reaction interacts with HEAC, then rising K likely lowers K_{TH} and increases da/dt compared to quasi-static loading, as observed in Figures 12 and 13. In such cases crack tip strain and strain rate are important variables.[13,49,75] Current results suggest that rising K at a sufficiently slow dK/dt provides identical (for susceptible alloy-environment conditions) to conservative (for resistant alloy-environment) values of HEAC threshold and kinetics.[13,49]

The HEAC properties in Figure 14, from elastoplastic K_J analysis of a small specimen, are quantitatively relevant to a structure under elastic loading, following the J-integral approach.[58,60,66,67,76–78] To verify this assertion, it is necessary to demonstrate K and J dominance of crack tip mechanics.[52] K dominance is established by comparing the uncracked SENT ligament (W–a) and plane strain plastic zone diameter (estimated using the Ramberg–Osgood flow properties for Monel K-500) for the deepest crack and high-elastic K of 50 MPa√m. For these conditions, the uncracked ligament is six times larger than the plastic zone diameter, suggesting that K governs crack tip stress and strain distributions, as supported by FEA analysis.[52] For elastoplastic deformation of a small specimen, J dominance requires (W–a) to be greater than MJ/σ_o, where M ranges from 25 to 200 for pure bending and tension, respectively.[79,80] At a K_J of 80 MPa√m, M is 100 and MJ/σ_o equals 3.9 mm for HEAC susceptible Monel K-500 with an uncracked ligament length of 6 mm. For HEAC resistant Monel K-500, with a typical uncracked ligament length of 9 mm, M is 175, and MJ/σ_o equals 6.8 mm. Even at this high K_J level, the criteria for J dominance are satisfied for the small SENT specimen under both HEAC resistant and susceptible conditions. Furthermore, the da/dt *vs* K relationships in Figure 14 demonstrate a classic Stage I–Stage II shape; loss of K or J dominance should cause a departure from this behavior.

Crack tip constraint similitude must also be considered when applying experimentally derived HEAC threshold and kinetics properties (Figure 14) in a component assessment. A plane strain continuum finite element analysis demonstrated that crack tip stress, strain, and dislocation-trapped $C_{H\text{-}Diff}$ fields in a small SENT specimen of an alloy steel (σ_o = 595 MPa and n = 17) stressed to K of 34 MPa√m in high pressure H_2 are well described by K and J.[52] Each field changed mildly as HEAC progressed from a low constraint condition at a/W of 0.08 ($T = -0.3\sigma_o$, where T is T-stress) to modest constraint ($T = +0.002\sigma_o$) at a/W of 0.6.[52] These constraint levels are typical of a small-surface crack subjected to tension or bending.

B. *HEAC Susceptibility of Monel K-500*

Aged Monel K-500 is susceptible to HEAC when stressed in NaCl solution at potentials substantially cathodic to the OCP of −200 to −250 mV_{SCE}. Crack growth rates (Figures 7, 9, and 14) and SEM analyses (Figures 8 and 10) show severe IG HEAC for $-1100\ mV_{SCE} < E_A < -850\ mV_{SCE}$, and slower but finite da/dt at −800 mV_{SCE} with slow-rising K. Polarization to either −700 or −750 mV_{SCE} eliminated resolvable IG HEAC for the loading rate investigated. Such cracking was also eliminated for static K loading at −800 mV_{SCE}.

The beneficial effect of reduced cathodic polarization is consistent with limited literature results. Slow strain rate tensile experiments in artificial seawater showed severe EAC at −1000[31] and −945 mV_{SCE},[2] high resistance at −850 mV_{SCE},[31] and possible immunity at −645 mV_{SCE}[2]; consistent with the fracture mechanics measurements in Figure 14 and Table III. Threshold stress intensity values for EAC in aged Monel K-500 (R_C 30 and σ_{YS} = 813 MPa) stressed in 3.5 pct NaCl solution were reported based on the rising step load (RSL) method.[28] K_{TH} ranged from 18.4 MPa√m at −1200 mV_{SCE} and 19.3 MPa√m at −1000 mV_{SCE}, to above 75 MPa√m at both −850 and −700 mV_{SCE}. This study did not report growth rates, the resolution of crack growth monitoring, the effect of plasticity on K_{TH}, or SEM analysis of EAC.[28]

These RSL results are consistent with the data in Table III for the higher levels of cathodic polarization; however, important differences are apparent. In the RSL experiment, K_{TH} was defined by a resolved load decrease due to crack extension during the static displacement

hold period. Crack growth during the rising K step was not considered. For highly negative E_A where HEAC is severe, current results show similar K_{TH} and da/dt for the step-load and slow-rising K formats; similar to the RSL data; in both methods K_{TH} ranges from 12 to 23 MPa$\sqrt{m}$ below -1000 mV_{SCE}. The K_{TH} levels are higher for potentials in the range of -850 to -700 mV_{SCE}, but the rising K experiments demonstrate HEAC at -800 mV_{SCE} and K_{TH} of 42 to 44 MPa$\sqrt{m}$ compared to the RSL implication of immunity for K up to 75 MPa$\sqrt{m}$.[28] There are two explanations for this difference. First, cracking may have occurred during the RSL test, but was not detected by load decrease if da/dt is low as suggested by the dcPD-based data in Figures 13 and 14. Second, HEAC can be promoted by concurrent plastic strain and H exposure, characteristic of the slow-rising K protocol, and absent during the RSL hold period. This issue is considered in an ensuing section.

C. *Stable-Ductile Crack Growth*

Aged Monel K-500 is susceptible to unexpected slow-stable crack growth below the reported K_{IC} range (Table II) for three conditions where IG HEAC did not occur. These conditions include: (a) slow-rising K loading in N_2, Figure 6; (b) slow-rising K in NaCl with cathodic polarization more positive than -750 mV_{SCE}, Figure 14; and (c) the step part of step-hold loading in NaCl at -800 mV_{SCE}, Figures 12 and 13. In each case da/dt exceeded the plasticity-based false rate and cracking occurred over a distance which is large compared to the calculated extent of crack tip blunting. Crack extension was TG for each set of conditions and progressed by dimple-based processes. Speculatively by elimination, the growth mechanism is crack tip creep plasticity at ambient temperature and promoted by slow-rising K. This suggestion is supported by the: (a) microvoid morphology, (b) lack of IG features, (c) high K_{IC} (Table II, 198 to 340 MPa$\sqrt{m}$) compared to the lower levels of applied K_J (< 100 MPa$\sqrt{m}$), (d) low-diffusible H concentration of as-received Monel K-500 (Table I heat) below the resolution limit of TDS measurement, and (e) very low H uptake during stressing in dry N_2 or in NaCl with low crack tip η_H.

Transgranular creep crack growth is outside the scope of this study, but may be pertinent to long-life damage tolerance of Monel components. Two points are notable. First, faster da/dt for the -700 and -750 mV_{SCE} NaCl cases (Figures 9 and 14) compared to cracking in N_2 suggests a lingering role of H in this plasticity-based environmental cracking. Second, the rate of slow-TG cracking appears to depend on dK/dt since da/dt values measured for rising K loading at -700 and -750 mV_{SCE} are substantially faster than the very slow rates recorded during the hold periods of the step-hold experiment at -800 mV_{SCE} (Figure 12).

D. *Mechanism Informed Modeling of IG HEAC Kinetics*

Model predictions of K_{TH} and da/dt will strengthen fundamental understanding of HEAC and reduce experimentation required to manage cracking.[13,43,52,72] Intergranular cracking in Monel K-500 stressed in chloride solution at cathodic potentials likely occurs by HEAC. Modeling requires input of the H concentration on the occluded crack tip surface in equilibrium with the local H overpotential, plus H delivered to the FPZ from uptake on bold-exposed surfaces. For Ni alloys, H production under cathodic polarization is greater on bold-exposed surfaces due to crack tip pH rise above bulk and less-cathodic crack tip potential from IR difference (Figure 2).[29,54] The decrease in crack tip *vs* bold surface production of $C_{H\text{-}Diff}$ is quantified as a function of E_A in Figure 5. However, the intensified 3-dimensional stress state at the crack tip and mid-plane of the SENT specimen dominates HEAC over boldly exposed surface locations. Full-bulk H charging during a 500,000 second experiment is not likely; the diffusion distance proportional to $2(D_H\, t)^{1/2}$ is 0.16 mm for the effective diffusivity of H in Monel K-500 (1.3×10^{-10} cm^2/s[29]). This H-penetration distance is only 13 pct of the half-thickness of the SENT specimen. In contrast diffusion of crack tip surface H into the FPZ likely occurs over a very short distance (~1 μm[13]) dictated by the crack tip stress field. Crack tip H uptake dominance is supported by SEM observations of uniform IG crack fronts with no preference for enhanced growth near boldly exposed surfaces (Figure 12(a)).

Stress-enhanced crack tip diffusible H concentration, $C_{H\sigma}$ given by Eq. [3], is used to predict K_{TH} (Eq. [1]) and da/dt_{II} (Eq. [2]) *vs* E_A for Monel K-500 in NaCl solution. For applied potentials between -1200 and -700 mV_{SCE}, the measured-diffusible H concentrations shown in Figure 4 and elsewhere[29] establish that C_L and C_{RT} in Eq. [3] are sufficiently low (<~0.003 atom fraction H) to justify $(1 - C_L)$ and $(1 - C_{RT})$ equaling 1. E_B for H in aged Monel K-500 is 10.2 ± 4.4 kJ/mol, associated with reversible H trapping at Ni_3Al precipitates.[29] As such, the exponential binding energy term in Eq. [3] is 55.2 and much greater than 1. With these simplifications Eq. [3] is:

$$C_{H\sigma} = \left[(1 - C_{L\sigma}) \exp\left(\frac{\sigma_H V_H}{RT}\right)\right]\left[C_L \exp\left(\frac{E_B}{RT}\right)\right]. \quad [10]$$

The value of crack tip σ_H used in the ensuing model yields a value of $C_{L\sigma}$ that is less than 0.050 to 0.10 atom fraction H for the most negative E_A investigated in the cracking experiments, assuming that C_L is 5 to 10 pct of $C_{H\text{-}Diff}$.[29] As such, $(1 - C_{L\sigma})$ is 0.90 to 0.95, justifying setting this term equal to 1. The second-bracketed exponential term in Eq. [10] is $C_{H\text{-}Diff}$ since $(1 - C_L)$ is also essentially 1. As such, Eq. [3] demonstrates that $C_{H\sigma}$ equals the exponential stress enhancement of experimentally determined $C_{H\text{-}Diff}$, which is established as a function of E_A in Figure 5 and Eq. [9].

E. *Threshold for HEAC*

Prediction of the applied potential dependence of the quasi-static K_{TH} for HEAC utilizes the crack tip micromechanical model by Gerberich *et al.*[41,81,82]

(Eq. [11]), based on H decohesion[83–85] and experimentally validated for a range of steels and a Ni-based superalloy.[42,43,82] The premise of this model is that near-crack-tip stress (and local stress intensity) is modeled by coupling a small array of dislocations, spaced in equilibrium with the crack tip elastic stress field, and including Rice–Thompson dislocation emission.[86] These dislocations shield the singular-elastic stress at the crack tip. Surrounding-tip plasticity is represented by a superdislocation located at the centroid of the highly strained continuum plastic zone, and related to stress intensity.[44,81,82] Crack tip stress of order 16 to 25 GPa is predicted for Fe-Si and Mo,[44] and is maximum at 20 to 100 nm ahead of the crack tip surface. This estimate is consistent with Oriani's original decohesion model.[83] Gerberich *et al.*[82] validated the crack tip dislocation-based model by showing that the H_2 pressure dependence of k_{IH} (equal to $(k_{IG} - \alpha C_{H\sigma})$) for a steel is consistent with the measured H_2 pressure dependence of the surface energy of iron (equal to $k_{IH}^2/2E$ according to the Griffith theory). Such data are not available for Ni or a superalloy.

Uncertain crack tip σ_H is a persisting issue in HEAC modeling. The value of σ_H/σ_{YS} used in Eq. [3] does not affect the ability of this approach to predict the E_A dependence of K_{TH} since σ_H/σ_{YS} inversely scales with the adjustable parameter, α, in Eq. [1]. The discrete dislocation model (maximum hydrostatic stress ~20 σ_{YS} at 20 to 100 nm beneath the crack tip)[41,81,82] and a blunted crack finite element model (maximum hydrostatic stress 3 to 5 σ_{YS} at 2 to 5 μm)[52,53] bound the crack tip stress field relevant for HEAC modeling. This latter hydrostatic stress may be increased if strain gradient plasticity impacts the crack tip stress distribution.[47,87] Moreover, TEM of the deformed crack wake in Ni and Fe shows that H promotes a dislocation cell structure that could provide increased crack tip stresses from work hardening to favor decohesion.[38,88–90] Based on these considerations, σ_H/σ_{YS} was assumed to equal 12.0. The values of α'' (0.00018 MPa m) and β' (0.26/MPa$\sqrt{m}$) in Eq. [1] were established by analytical approximation to the dislocation simulations of the near-crack-tip stress field,[41,81,82] and validated by experiment.[43] The intrinsic Griffith toughness of the IG interface without H, k_{IG}, is not physically related to K_{IC} for microvoid fracture (198 to 340 MPa$\sqrt{m}$; Table II) or to the K levels that caused TG creep crack growth in Monel K-500 (60 to 80 MPa$\sqrt{m}$, Figure 6). Rather, k_{IG} was equated to 0.675 MPa$\sqrt{m}$ so as to predict K_{TH} of 100 MPa$\sqrt{m}$ when $C_{H\text{-}Diff} = 0$. This is a reasonable-lower bound since IG cracking was not observed for K_I up to this value for E_A that produced $C_{H\text{-}Diff}$ near 0. The α was set to 0.56 (MPa$\sqrt{m}$ per atom fraction H) to fit the model to the average of three K_{TH} values (18.0 MPa$\sqrt{m}$) measured at E_A of −1000 mV_{SCE}.

With these input parameters, Figure 15 demonstrates that Eq. [1] predicts the dependence of K_{TH} on the fundamentally important stress-enhanced concentration of H in the crack tip FPZ ($C_{H\sigma}$, top axis), as well as on the $C_{H\text{-}Diff}$ associated with the occluded crack tip η_H (bottom axis). Predicted and measured K_{TH} agree, and each decreases strongly with initial increase in $C_{H\text{-}Diff}$ (and $C_{H\sigma}$) to reach a lower limit at high H concentrations. The model also successfully predicts the strong dependence of K_{TH} on applied potential, as shown in Figure 16. Figure 5 and Eq. [9] show that crack tip $C_{H\text{-}Diff}$ extrapolates to 0 at an applied potential of −764 mV_{SCE}. The model predictions in Figure 16 show that K_{TH} approaches the H-free toughness at this level of E_A and associated $C_{H\text{-}Diff}$ of 0. Experiments (Figures 9 through 11) established that HEAC occurred at −800 mV_{SCE}, but not at −750 or −700 mV_{SCE}. The impact of a 50 pct higher α (0.83 MPa$\sqrt{m}$ per atom fraction H), and 50 pct lower α (0.37 MPa$\sqrt{m}$ per atom fraction H), is shown by the dashed lines in Figures 15 and 16 with other parameters held constant.

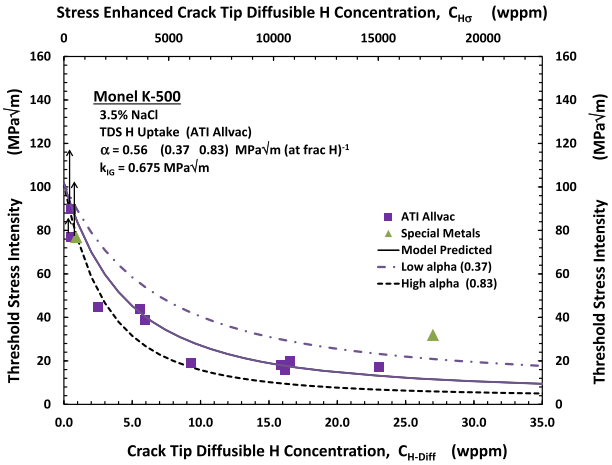

Fig. 15—(Color online) Model predicted (Eq. [1]) and measured (Table III) K_{TH} *vs* occluded crack tip $C_{H\text{-}Diff}$ (bottom axis) and stress-enhanced $C_{H\sigma}$ (top axis) for aged Monel K-500 (ATI Allvac, ■; Table I) stressed in 3.5 pct NaCl at E_A between −1100 and −700 mV_{SCE}. The relationship between $C_{H\text{-}Diff}$ and applied potential is given by Eq. [9] and σ_H/σ_{YS} equals 12.0 in Eq. [3]. Measured K_{TH} are included for a second lot of aged Monel K-500 (Special Metals, ▲; Footnote *) using the corresponding H uptake law (Footnote **).

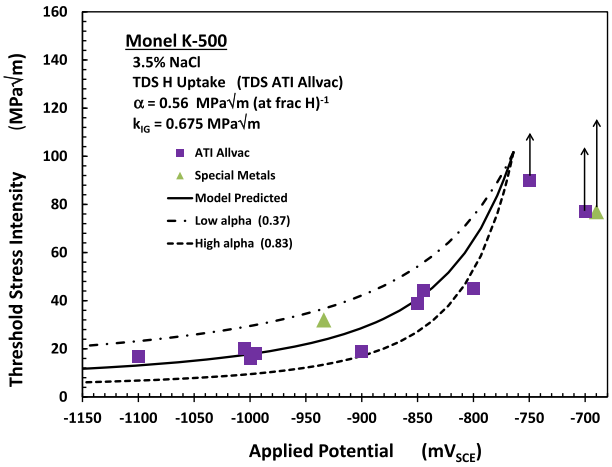

Fig. 16—(Color online) Model predicted (Eq. [1]) and measured (Table III) K_{TH} for HEAC *vs* E_A for aged Monel K-500 (ATI Allvac, ■; Table I) stressed in 3.5 pct NaCl. The σ_H/σ_{YS} is 12.0 in Eq. [3]. Measured K_{TH} are included for a second lot of aged Monel K-500 (Special Metals, ▲; Footnote *).

The values of the parameters used for the fits shown in Figures 15 and 16 are justified based on previous applications of this model and in the previous paragraphs. The precise k_{IG} used for grain boundary "brittle fracture" is important, but the choice does not affect the conclusion that the K_{TH} model is validated. As an example, k_{IG} of 0.72 MPa$\sqrt{m}$ corresponds to a macroscopic interface toughness of 160 MPa$\sqrt{m}$. An α of 0.68 MPa$\sqrt{m}$ per atom fraction H, with this higher k_{IG}, provides a similar-good fit to the experimental data as that shown in Figures 15 and 16. The precise crack tip stress distribution and associated H trapping (Eq. [3]) does not alter the conclusion that the present approach predicts the E_A dependence of K_{TH}. The good fits shown in Figures 15 and 16 are preserved if the blunted crack tip value of σ_H/σ_{YS} of 4.0 is employed in place of σ_H/σ_{YS} equaling 12.0 to estimate $C_{H\sigma}$ through Eq. [3].[52] The corresponding best fit α is 26.2 MPa$\sqrt{m}$ per atom fraction H, calibrated by measured K_{TH} for E_A of -1000 mV_{SCE}. The higher σ_H/σ_{YS} of 12.0 calculation is favored as consistent with the discrete dislocation basis of Eq. [1][41] and local dislocation structure hardening.[38,88–90]

Modeling of K_{TH} *vs* applied potential depends on the input values of crack tip $C_{H\text{-}Diff}$ *vs* E_A (Figure 5 and Eq. [9]). It is uncertain as to whether crack tip H uptake is determined by x^2/G scaling, as done for the modeling in Figures 15 and 16, or by x/G scaling; however, the former dependence is justified.[54] If crack chemistry and H uptake are governed by x/G, then the relationship between crack tip $C_{H\text{-}Diff}$ and E_A given by the dashed line in Figure 5 and Eq. [9] shifts to a lower H concentration at each E_A. The absolute value of this concentration reduction is about a factor of 2 based on x/G correlation over the relevant range from 90 to 200. Identically good agreement between model predicted and measured K_{TH} (Figures 15 and 16) is achieved by raising the fitting parameter, α, in direct proportion to this lowering of $C_{H\text{-}Diff}$ such that $\alpha C_{H\sigma}$ is constant, as shown by Eqs. [1] and [3]. Similarly, the planar electrode $C_{H\text{-}Diff}$ dependence on E_A depends on the method used for H analysis (Figure 4). For this study and a separate investigation of a different lot of Monel K-500,[29] diffusible H concentration from the barnacle cell measurement was consistently less than that from hot extraction-calibrated TDS. This reduction factor is 3.4 at -1000 mV_{SCE} for the data in Figure 4 and 4.7 for the previous study.[29] If this difference is constant at each potential in Figure 4, then use of the barnacle cell-based H uptake dependence on E_A will not affect the quality of predicted *vs* measured K_{TH} in Figures 15 and 16. However, the absolute value of α necessary to fit the data at E_A of -1000 mV_{SCE} rises inversely with decreasing planar electrode $C_{H\text{-}Diff}$.

HEAC in a second lot of Monel K-500 (Footnote *) is represented (▲) in Figures 15 and 16. K_{TH} for this alloy was very high at -700 mV_{SCE}, consistent with the fall in $C_{H\text{-}Diff}$ to 0 near this potential. For each lot of Monel K-500, measured and model predicted K_{TH} agree when plotted *vs* E_A (Figure 16); however, this is misleading. The $C_{H\text{-}Diff}$ is consistently 2.3 times higher in the second lot of Monel K-500 for a given applied potential (Footnote **[29]) compared to the heat studied in the present work (Table III). Comparison based on E_A, is therefore not a fundamentally correct way to view the behavior of these two lots of Monel K-500 since crack tip diffusible H varies. The comparison in Figure 15 includes the correct H uptake law for the ATI Allvac lot (Figure 4) and the Special Metals lot (Footnote **) in the calculation of crack tip $C_{H\text{-}Diff}$. On this correct basis, the two lots of Monel K-500 are not well described by a single set of model constants. The trend in Figure 15 for α = 0.56 MPa$\sqrt{m}$ per atom fraction H is shifted to intersect the two values of K_{TH} (▲) for the Special Metals lot of Monel K-500 by changing α to = 0.27 MPa$\sqrt{m}$ per atom fraction H for k_{IG} = 0.675 MPa$\sqrt{m}$. This difference in α implies that these two lots of Monel K-500 are intergranularly embrittled to a different extent by the same $C_{H\sigma}$, suggesting a metallurgical effect on HEAC. This speculation, or a parallel explanation quantified by alloy-sensitive change in k_{IG}, must be verified and the governing microstructure-composition factor(s) identified.

Good agreement between measured and model predicted dependencies of K_{TH} on applied potential supports the conclusion that a critical level of cathodic polarization must be exceeded before HEAC can progress at a significant rate in Monel K-500 stressed in NaCl. With a single-calibration parameter, α, the model quantitatively captures the E_A dependence of K_{TH} in spite of uncertainties associated with crack tip stress and H uptake. Refinement of either factor only changes the absolute value of α, which is a weighting parameter that quantifies the sensitivity of a grain boundary to decohesion for a given $C_{H\sigma}$. The α that governs HEAC should depend on metallurgical factors such as boundary chemistry, structure, and slip interaction. The absolute value of α is important if this factor is interpreted based on a first principles model of boundary-H decohesion.

F. *Stage II Crack Growth Rate*

Knowing the relationship between E_A and crack tip diffusible H concentration ($C_{H\text{-}Diff}$ scaled to $C_{H\sigma}$), it is possible to predict the E_A dependence of da/dt_{II} based on HEAC rate limited by H diffusion in the FPZ.[45] Equation [2] predicts da/dt_{II} using a single adjustable parameter, $C_{H\sigma\text{-}crit}$, with all other terms in this model independently known. The D_H for H in aged Monel K-500 at 298 K (25 °C) was reported as 5×10^{-11} cm^2/s,[48] 1.5 to 1.9×10^{-10} cm^2/s,[24] and 9×10^{-11} to 4×10^{-10} cm^2/s[29]; a H diffusivity of 1×10^{-10} cm^2/s is used. The applied potential dependence of $C_{H\text{-}Diff}$ for x^2/G relevant to an SENT crack is given in Figure 5 and Eq. [9] for ATI Allvac Monel K-500. The x_{crit} in Eq. [2] is 1 μm for HEAC in a wide range of high strength alloys.[43,45] The crack tip σ_H in Eq. [3] is assumed to be 12 σ_{YS}, consistent with x_{crit} of 100 to 1000 nm as justified for the K_{TH} model.

Model predictions of Stage II crack growth rate are presented in Figures 17 and 18, using an adjustable best fit $C_{H\sigma\text{-}crit}$ of 1100 wppm. Predicted and measured (Table III) da/dt_{II} agree when considered as a function of either crack tip diffusible H concentration (Figure 17, bottom axis),

stress-enhanced concentration of H at the crack tip ($C_{H\sigma}$, top axis) or applied cathodic potential (Figure 18).[§]

[§]Measured da/dt_{II} values in Figures 17 and 18 include results for the Special Metals lot of aged Monel K-500 (Footnote *, ▲). The modified H uptake relationship (Footnote **) was used to define $C_{H\sigma}$ so the prediction in Figure 17 is valid. The good agreement with the da/dt_{II} model prediction in Figure 18 is due to the predicted insensitivity of da/dt_{II} to the 2.3 times higher $C_{H\text{-}Diff}$ for the Special Metals alloy at a given E_A.

The fastest Stage II crack growth rate measured at E_A of -1100 mV_{SCE}, 0.17 μm/s, agrees with Eq. [2] when $C_{H\sigma} \gg C_{H\sigma\text{-}crit}$, and this model suggests that more severe cathodic polarization will only cause a small-additional increase in da/dt_{II}. Specifically, the squared inverse error function term in Eq. [2] equals 1.04 when $C_{H\sigma} = 7\ C_{H\sigma\text{-}crit}$ (7700 wppm H) and 4.8 when $C_{H\sigma} = 500\ C_{H\sigma\text{-}crit}$ (550,000 wppm H). For this range of $C_{H\sigma}/C_{H\sigma\text{-}crit}$, the predicted Stage II crack growth rate from Eq. [2] equals 4.2 to 19.2 times (D_H/x_{crit}), or 0.04 to 0.19 μm/s for D_H of 1.0×10^{-10} cm^2/s.

Good agreement between measured and modeled da/dt_{II} affirms the validity of HEAC in Monel K-500 as rate limited by H diffusion within the 1 μm crack tip FPZ. This model prediction relies on a single-calibration parameter, $C_{H\sigma\text{-}crit}$, which is referenced in the context of $C_{H\sigma}$ governed by occluded crack tip η_H and crack tip hydrostatic stress enhancement. The squared inverse error function of the concentration term of $(1 - C_{H\sigma\text{-}crit})/C_{H\sigma}$ dictates the shallow decrease in da/dt_{II} with decreasing H concentration (increasing E_A). The somewhat steeper decline in measured growth rates may be speculatively explained by a modest decrease of D_H with decreasing $C_{H\text{-}Diff}$ (increasing E_A) due to reversible H trapping at dislocations or γ'.[50] The model prediction in Figures 17 and 18 used a constant D_H. The inverse error function term also controls the technologically important potential dependence of da/dt_{II} where growth rate plummets with further small rise in applied potential above a critical value. This sharp reduction in da/dt_{II} is accompanied by a transition from IG HEAC (at -800 mV_{SCE}, Figure 10) to ductile cracking (at -750 and -700 mV_{SCE}, Figure 11). For the parameters employed and $C_{H\sigma\text{-}crit} = 1100$ wppm, this severe drop-off in HEAC da/dt_{II} is predicted to occur at E_A above -810 mV_{SCE}, in excellent agreement with the measurements in Table III. Specifically, for increasing E_A from -810 to -787 mV_{SCE} in Figure 18, crack tip $C_{H\text{-}Diff}$ falls from 3.2 to 1.6 wppm ($C_{H\sigma}$ falls from 2060 to 1023 wppm, Figure 17 for $\sigma_H/\sigma_{YS} = 12.0$) and the squared inverse error function term in Eq. [2] decreases from 0.19 to 5×10^{-7}. This concentration term in the diffusion model causes the predicted seven order of magnitude decrease in da/dt_{II} for a 23 mV increase in E_A. Experiments established that IG HEAC was produced at -800 mV_{SCE} (Figure 10) with the rate plotted in the upper plateau of Figures 17 and 18. SEM analysis did not resolve HEAC for the experiments at either -750 or -700 mV_{SCE} and for K_J up to 80 MPa$\sqrt{m}$ (Figure 14).

The specific value of $C_{H\sigma\text{-}crit}$ affects the predicted potential for the strong decrease in da/dt_{II}, but not the maximum da/dt_{II} which is achieved at more negative potentials. Model sensitivity analysis provides the critical levels of E_A necessary to eliminate HEAC for various assumed $C_{H\sigma\text{-}crit}$ values: 275 wppm and -770 mV_{SCE}, 550 wppm and -777 mV_{SCE}, 1100 wppm and -787 mV_{SCE} (Figure 18), 2200 wppm and -814 mV_{SCE}, 4400 wppm and -865 mV_{SCE}, and 6600 wppm and -910 mV_{SCE}. Steep reductions in da/dt_{II} are predicted for this wide range of assumed $C_{H\sigma\text{-}crit}$.[§§] This analysis

[§§]Listed values of $C_{H\sigma\text{-}crit}$ are relative to $C_{H\sigma}$ which was stress enhanced by a factor of 650 (Eq. [3]) for Monel K-500 with $\sigma_{YS} = 773$ MPa and $\sigma_H = 12\sigma_{YS}$. In the context of stress-free $C_{H\text{-}Diff}$, critical H concentrations for da/dt_{II} falloff vary from 10.1 to 0.4 wppm for this sensitivity analysis.

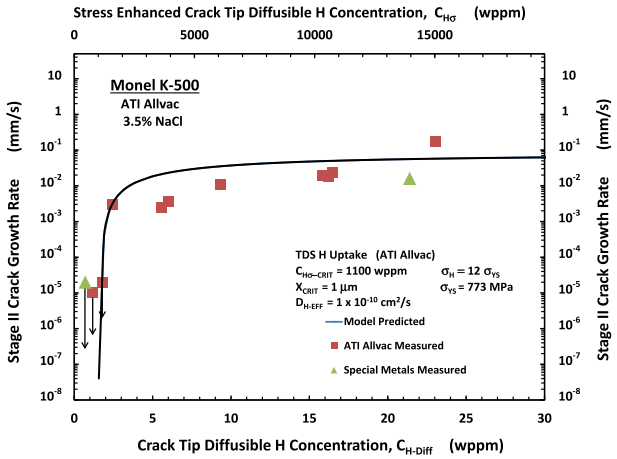

Fig. 17—(Color online) Model predicted (Eq. [2]) and measured Stage II crack growth rate (at elastic $K = 50$ MPa$\sqrt{m}$; Table III; Fig. 9) *vs* crack tip $C_{H\text{-}Diff}$ (bottom axis) and stress-enhanced $C_{H\sigma}$ (top axis) for aged Monel K-500 (ATI Allvac, ■; Table I) stressed in 3.5 pct NaCl at E_A between -1100 and -700 mV_{SCE}. The σ_H/σ_{YS} is 12.0 in Eq. [3]. Measured da/dt_{II} are included for a Special Metals lot of Monel K-500 (▲) using the corresponding H uptake law (Footnotes * and **).

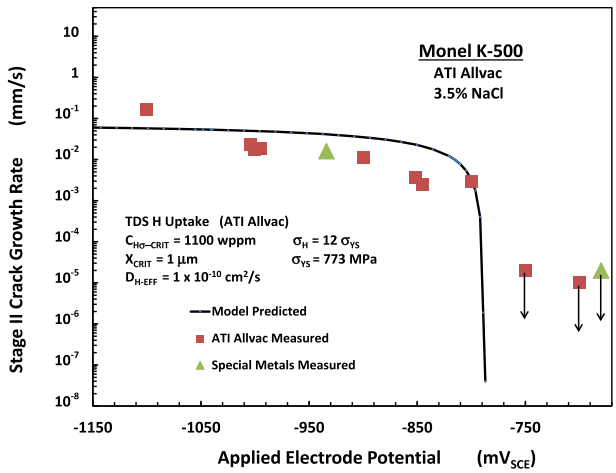

Fig. 18—(Color online) Model predicted (Eq. [2]) and measured Stage II crack growth rate (at elastic $K = 50$ MPa$\sqrt{m}$; Table III; Fig. 9) *vs* applied cathodic potential for aged Monel K-500 (ATI Allvac, ■; Table I) stressed in 3.5 pct NaCl. The σ_H/σ_{YS} equals 12.0 in Eq. [3]. Measured da/dt_{II} values are included for a Special Metals lot of Monel K-500 (Footnote *,▲).

supports the expectation that HEAC occurs when applied cathodic polarization is more negative than a potential in the range of −770 to −900 mV_{SCE}. The precise potential may depend on subtle differences in Monel metallurgy effects on $C_{H\sigma\text{-crit}}$ and the H uptake law. This variation in critical potential, coupled with the conservative characterization of HEAC resistance provided by the slow-rising K method (discussed in the next section), are important considerations when predicting IG EAC in a component.

G. *Effect of Loading Protocol*

The results for HEAC in Monel K-500 suggest a strong effect of loading protocol, depending on applied potential. Similar rates of IG HEAC were produced for slow-rising K and quasi-static K loading, but only when cracking was relatively severe at E_A below about −900 mV_{SCE}. These kinetics of IG HEAC are governed by applied K, and the associated crack tip stress and strain fields, independent of crack growth or K history. In contrast for milder cathodic polarization (E_A above −900 to −800 mV_{SCE}) and lower $C_{H\text{-}Diff}$, IG HEAC occurred for slow-rising stress intensity loading with a substantial amount of TG cracking present (Figure 10). However, da/dt was near-zero (Figure 13) for constant K during a hold period after a fast-step rise in K and IG HEAC was eliminated (Figure 12). A similar result was reported for HEAC in IN718.[14] For alloys in aqueous environments, the damaging effect of slow-rising K may be ascribed to the effect of crack tip strain and strain rate on crack surface film stability and reactivity leading to increased H uptake.[75,91] Slow-rising K similarly lowered the threshold for hydrogen embrittlement of steel, either stressed in pure H_2,[49] or precharged with H then stressed in air.[13] For these cases, the different behavior of a stationary crack under rising K *vs* a propagating crack under fixed or falling K is related to interaction of FPZ stress, plastic strain, and trapped H leading to "plasticity-related hydrogen induced cracking" (PRHIC).[49,92,93]

It is not possible to establish the cause of the loading format effect on HEAC of Monel K-500. A role of crack tip plasticity is suggested by slip traces on grain facets (Figure 8), as well as by Transmission Electron Microscopy (TEM) observations of H-affected crack tip dislocation structure in Ni.[38] Speculatively, highly localized slip, perhaps intensified by H interaction with moving dislocations,[94,95] impacts grain boundaries during strain accumulation. This plasticity could promote grain boundary decohesion by providing microscopic stress concentration and H enrichment at dislocation-generated trap sites including: altered grain boundary structure,[38] adjacent cell interface structure,[89,90,96] plasticity-boundary carbide interaction,[97] or grain boundary microvoids.[98,99] Moreover, as E_A becomes more positive above about −900 mV_{SCE}, TG HEAC occurs and may involve H damage associated with slip band and twin band intersections.[14,100] PRHIC in steels[13,49] and Ni alloys appears to be most severe (lowest-intrinsic K_{TH} and fastest da/dt) when crack tip strain and crack tip H accumulate concurrently. Cracking is less severe when plastic strain accumulates before H exposure, or when crack propagation during H exposure lowers the severity of the crack tip strain field.[49] These concepts are used to examine the loading format effect on HEAC in Monel K-500. The approach taken is based on blunt-crack continuum mechanics and plastic strain-based failure, rather than the decohesion-based models of K_{TH} and da/dt_{II} used for higher $C_{H\text{-}Diff}$ (Figures 15 through 18).

The ratio of K_{TH} for the onset of HEAC under slow-rising K (K_{THi}) to the threshold for crack arrest (K_{THa}) during propagation under falling K appears to provide an indicator of the importance of loading format. Continuum analysis of the effect of crack propagation on the strength of the crack tip strain singularity yielded[49]:

$$\frac{K_{THa}}{K_{THi}} = (A')\frac{\left[\exp\left(\varepsilon_f^H/\varepsilon_o\right)\right]^B}{\sqrt{\left(\varepsilon_f^H/\varepsilon_o\right)}}, \qquad [11]$$

where ε_f^H is the H-sensitive crack-tip effective-plastic strain at fracture, ε_o is yield strain (0.004 for H-free Monel K-500), and A' ($\sqrt{\pi}$) and B (0.3) are constants from analysis of an elastic-perfectly plastic solid.[101] While this model centers on critical strain, the H damage mechanism can involve stress controlled interface decohesion with local fracture stress directly related to ε_f^H. For HEAC in IN718, ε_f^H was experimentally determined using locally measured dimple size in two void growth models, then correlated with occluded crack $C_{H\text{-total}}$, each as a function of bulk solution pH.[14] Specifically, ε_f^H decreases monotonically with increasing H concentration:

$$\sqrt{\varepsilon_f^H} = \left(0.19 - 2.38 \times 10^{-3} C_{H-total}\right), \qquad [12]$$

where $C_{H\text{-total}}$ (wppm, over the range from 0 to 40 wppm) was estimated as the value in equilibrium with crack tip pH and potential, but not stress-enhanced analogous to Eq. [9] for Monel K-500. A similar result was reported for H cracking of IN903.[100] A loading format effect on HEAC is expected when K_{THa}/K_{THi} (Eq. [11]) exceeds unity, as is likely when ε_f^H (Eq. [12]) rises due to increasing H-free alloy ductility or reduced H uptake.

Equations [11] and [12] provide the basis to interpret the observed loading format effect on HEAC in Monel K-500 stressed in NaCl. Equation [9] shows that $C_{H\text{-}Diff}$ falls from 23 to 2.5 wppm for $-1100\ mV_{SCE} < E_A < -800\ mV_{SCE}$, and Figure 4 shows $C_{H\text{-total}} \sim 1.2C_{H\text{-}Diff}$, which is typical of Ni-based superalloys.[29] Assuming that Eq. [12] is relevant for Monel K-500, with $\varepsilon_o = 0.004$, this decrease in $C_{H\text{-total}}$ results in increased $\varepsilon_f^H/\varepsilon_o$ from 7.7 to 16.7. From Eq. [11], these changes in $\varepsilon_f^H/\varepsilon_o$ yield K_{THa}/K_{THi} of 2.8 at −1100 mV_{SCE}, 7.6 at −800 mV_{SCE}, and 650 or higher for E_A of −760 mV_{SCE} and above. The trend predicted by this analysis is consistent with the HEAC loading format effect for Monel K-500. However, for this model to precisely fit with the HEAC experiments, the predicted K_{THa}/K_{THi} at −1100 mV_{SCE} should be 1, rather than 2.8. Two issues preclude quantitative determination of K_{THa}/K_{thi} *vs* $C_{H\text{-total}}$. First, the relevance of Eq. [12] to Monel K-500 is not verified and a modest change in $\varepsilon_f^H/\varepsilon_o$

strongly impacts K_{THa}/K_{THi}. Second, A' and B in Eq. [11] are approximate for a work hardening alloy such as Monel K-500. The K_{THa}/K_{THi} should decrease due to work hardening, compared to the Eq. [11] prediction.[49,101] Work is required to better quantify this crack tip mechanics analysis for Ni superalloys, as well as to establish the physical basis for the contributions of enhanced H uptake, trap generation, and local work hardening unique to concurrent plasticity and H accumulation.

The difference in the HEAC susceptibility of Monel K-500, subjected to rising step and hold loading compared to continuous-rising K, is understood based on damage from interaction of crack tip plasticity and H. An experiment, which produces sequential plastic strain followed by H accumulation, is less potent in terms of producing HEAC compared to slow-concurrent accumulation of strain and H. For RSL, H does not accumulate during the fast-rising-K step when strain accumulates, and crack tip strain does not accumulate during the hold (other than by low-rate creep) when H accumulates. With nil-concurrent plastic strain and H accumulation at intermediate cathodic polarization, $C_{H\sigma}$ is low and ε_f^H is high; PRHIC does not occur at a measurable rate. In contrast modest TG HEAC occurs during concurrent crack tip plastic strain and H accumulation characteristic of continuous-rising K loading. For substantial cathodic polarization, crack tip H concentration is high and ε_f^H is low to favor HEAC, which occurs similarly for concurrent (slow-rising K) as well as sequential (RSL) crack tip plasticity and H accumulation.

Stress corrosion cracking in a Monel K-500 component depends on the interaction of loading protocol and level of cathodic polarization. Slow-rising K with precision-continuous detection of crack growth provides K_{TH} and da/dt which are accurate to conservative for a given cathodic polarization. If a component is quasi-statically loaded such that plasticity accumulation is low during H uptake, or vice versa, then HEAC growth may be less than that projected based on the rising K experiment. This difference is important at intermediate levels of cathodic polarization where crack tip H concentration is low to moderate. The present results show that significant HEAC is expected for aged Monel K-500 components stressed under slow-rising load at potentials in the range of $-800\ mV_{SCE} < E_A < -750\ mV_{SCE}$. However, this "critical potential" regime is likely lower (more cathodic) for a statically loaded component such as a torqued fastener. This expectation should be compared to detailed analysis of the level of cathodic polarization for a crack location in a bare or painted Monel component coupled with zinc.

V. CONCLUSIONS

- The slow-rising stress intensity method, with dcPD monitoring of a small crack, provides a quantitative-accelerated characterization of environmental cracking when enhanced to account for crack surface electrical contact, crack tip plasticity, and small-specimen ligament plasticity through J-integral analysis.
- Aged Monel K-500 is susceptible to severe IG HEAC in NaCl solution when cathodically polarized at $-800\ mV_{SCE}$ and lower, concurrent with slow-rising stress intensity. Cracking is eliminated by cathodic polarization in the range of $-750\ mV_{SCE}$ and above.
- Occluded crack tip diffusible H concentration rises with increasing cathodic polarization from -750 to $-1100\ mV_{SCE}$, quantified for aged Monel K-500 by: (a) effective H solubility measured *vs* H overpotential on a planar electrode, and (b) measured-local crevice potential and pH geometrically scaled to a crack tip. Crack tip H concentration falls to near-0 wppm for bold-surface potentials above $-765\ mV_{SCE}$.
- Experimentally measured and predicted dependencies of K_{TH} and da/dt_{II} on crack tip diffusible H concentration (and applied cathodic potential) are in excellent agreement, validating these H decohesion-based models including dislocation-shielded high crack tip stress and a 1-μm scale crack tip process zone. A single experimentally calibrated parameter is required for each model.
- Cathodic polarization, more negative than $-765\ mV_{SCE}$, is required to cause HEAC in Monel K-500 for rising K loading. The H concentration dependent term in the diffusion model for da/dt_{II} explains a 5 to 10 order of magnitude increase in HEAC growth rate, over a narrow range of increasingly cathodic potential.
- HEAC in Monel K-500 is exacerbated by slow-rising K, which favors concurrent H exposure and crack tip strain accumulation compared to quasi-static loading. This loading protocol effect is increasingly important for moderate to low H uptake and increasing alloy fracture strain.
- The critical potential is likely more cathodic than $-800\ mV_{SCE}$ for quasi-static loading and/or increasing alloy resistance to HEAC; depending on the H uptake relationship plus key parameters in the models for K_{TH}, da/dt_{II}, and plasticity-based HEAC.
- When HEAC does not occur due to low H uptake, aged Monel K-500 may be susceptible to slow-rate TG cracking, perhaps creep crack growth.

ACKNOWLEDGMENTS

This research was sponsored by ONR Grants N00014-06-1-0366 and N00014-10-1-0552 with Dr. Airan Perez as Scientific Officer. Fracture mechanics experiments were conducted by Mr. Yongwon Lee and Mr. Justin Dolph at the University of Virginia, Mr. J. Keith Donald at Fracture Technology Associates, and Dr. Matthew A. Adler at Westmoreland Mechanical Testing and Research. These contributions are acknowledged.

REFERENCES

1. K.D. Efird: *Mater. Perform.*, 1985, vol. 24, pp. 37–40.
2. L.H. Wolfe and M.W. Joosten: *SPE Prod. Eng.*, 1988, vol. 3, pp. 382–86.
3. L.H. Wolfe and C.C. Burnette: *Document 20294-MS*, Society of Petroleum Engineers, 1990. (http://www.onepetro.org/mslib/servlet/onepetropreview?id=00020294).
4. M.W. Joosten and L.H. Wolfe, *Offshore Technology Conference Paper No. 5553-MS*, April, 1987.
5. L.H. Wolfe, C.C. Burnette, and M.W. Joosten: *Corrosion 93*, Paper No. 288, NACE International, Houston, TX, 1993.
6. G.A. Scott: *17th Offshore Technology Conference*, Paper No. OTC 5050, Houston, TX, 1985.
7. R.E. Butler: *Engineering with Copper-Nickel Alloys*, Metals Society, London, 1988, pp. 79–84.
8. L.H. Wolfe, C.C. Burnette, and M.W. Joosten: *Mater. Perform.*, July, 1993, pp. 14–21.
9. C.A. Clark, S. Driscoll, and P. Guha: *Br. Corros. J.*, 1997, vol. 27, pp. 157–60.
10. J.R. Scully and M.G. Vassilaros: *The Hydrogen Embrittlement Susceptibility of Monel Alloy K-500, Report DTNSRDC/SME-84-69*, David Taylor Naval Ship Research and Development Center, Bethesda, MD, 1984.
11. R. Bayles, T. Lemieux, F. Martin, D. Lysogorski, T. Newbauer, W. Hyland, B. Green, E. Hogan, T. Longazel and P. Stencel: *Naval Surface Treatment Center MR2010 Proceedings Presentation*, 2010. (http://www.nstcenter.com/docs/PDFs/MR2010/Thurs-1-Presentations/10-Bayles.PDF).
12. H.R. Copson and C.F. Cheng: *Corrosion*, 1956, vol. 12, pp. 647–53.
13. R.P. Gangloff: in *Comprehensive Structural Integrity*, I. Milne, R.O. Ritchie, and B. Karihaloo, eds., Elsevier, New York, NY, vol. 6, pp. 31–101, 2003.
14. J.A. Lillard: Ph.D. Dissertation, University of Virginia, Charlottesville, VA, 1998.
15. R.B. Rebak: in *Environment Induced Cracking of Materials (EICM-2)*, S.A. Shipilov, R.H. Jones, J.-M Olive, and R.B. Rebak, eds., Elsevier, Oxford, pp. 435–46, 2007.
16. R.H. Jones and S.M. Bruemmer: in *Environment Induced Cracking of Metals*, R.P. Gangloff and M.B. Ives, eds., NACE, Houston, TX, pp. 287–310, 1990.
17. M.H. Kamdar: *Second International Congress on Hydrogen in Metals*, P. Azou, ed., Paper No. 3D10, Pergamon Press, Oxford, pp. 1–11, 1977.
18. D.H. Lassila and H.K. Birnbaum: *Acta Metall.*, 1987, vol. 35, pp. 1815–22.
19. D.H. Lassila and H.K. Birnbaum: *Acta Metall.*, 1988, vol. 36, pp. 2821–25.
20. R. Otsuka, T. Maruno, and H. Tsuji: *International Congress on Metallic Corrosion*, National Research Council, Canada, 1984, vol. 2, pp. 270–77.
21. N.R. Moody, S.L. Robinson, and W.M. Garrison, Jr: *Res. Mech.*, 1990, vol. 30, pp. 143–206.
22. D.M. Symons: *Eng. Fract. Mech.*, 2001, vol. 68, pp. 751–71.
23. J.L. Mihelich and A.R. Troiano: *Nature*, 1963, vol. 197, pp. 996–97.
24. J.A. Harris, R.C. Scarberry, and C.D. Stephens: *Corrosion*, 1972, vol. 28, pp. 57–62.
25. D.M. Aylor: *Proceedings of the 1992 Tri-Service Corrosion Conference*, M. Levy, ed., AMPTIAC Document No. AMO26091, 1992.
26. C.E. Price and R.S. Fredell: *Metall. Trans. A*, 1986, vol. 17A, pp. 889–98.
27. A.W. Funkenbush, L.A. Heldt, and D.F. Stein: *Metall. Trans. A*, 1982, vol. 13A, pp. 611–18.
28. L. Raymond: *Fracture and Stress Corrosion Cracking Resistance of C465, BioDur 108, SpT 13-8, K-Monel 500, and Zeron 100, Report #CTC'071024*, L. Raymond and Associates, Newport Beach, CA, 2008.
29. J. Ai, H. Ha, R.P. Gangloff, and J.R. Scully: *Acta Mater.*, 2013, vol. 61, pp. 3186–99.
30. M.G. Vassilaros, R.L. Juers, M.E. Natishan, and A.K. Vasudevan: in *Slow Strain Rate Testing for Evaluation of Environmentally Induced Cracking Research and Engineering Applications, ASTM STP 1210*, R.D. Kane, ed., ASTM International, West Conshohocken, PA, pp. 123–33, 1993.
31. M.G. Koul and P. S. LeGrand: *Corrosion 2011*, Paper No. 11296, NACE International, Houston, TX, 2011.
32. M.A. Natishan and W.C. Porr, Jr.: in *Structural Integrity of Fasteners, ASTM STP 1236*, P.M. Toor, ed., ASTM International, West Conshohocken, PA, 1995, pp. 81–92.
33. S. Bechtle, M. Kumar, B.P. Somerday, M.E. Launey, and R.O. Ritchie: *Acta Mater.*, 2009, vol. 57, pp. 4148–57.
34. S. Lynch: in *Gaseous Hydrogen Embrittlement of Materials in Energy Technologies*, R.P. Gangloff and B.P. Somerday, eds., Woodhead, Cambridge, 2012, vol. 1, pp. 274–346.
35. Y.D. Park, D.L. Olson, A. Landau, and M. Pinkas: *Corrosion*, 2006, vol. 62, pp. 395–402.
36. T. Boniszewski and G.C. Smith: *Acta Metall.*, 1963, vol. 11, pp. 165–78.
37. M.L. Wayman and G.C. Smith: *Acta Metall.*, 1971, vol. 19, pp. 227–31.
38. M.L. Martin, B.P. Somerday, R.O. Ritchie, P. Sofronis, and I.M. Robertson: *Acta Mater.*, 2012, vol. 60, pp. 2739–45.
39. Z. Guo, M. Zhao, C. Li, S. Chen, and L. Rong: *Mater. Sci. Eng. A*, 2012, vol. 555, pp. 77–84.
40. Y. Fukai: *J. Alloys Compd.*, 2003, vols. 356–7, pp. 263–69.
41. W.W. Gerberich: in *Gaseous Hydrogen Embrittlement of Materials in Energy Technologies*, R.P. Gangloff and B.P. Somerday, eds., Woodhead, Cambridge, 2012, vol. 1, pp. 209–46.
42. Y. Lee and R.P. Gangloff: *Metall. Mater. Trans. A*, 2007, vol. 38A, pp. 2174–90.
43. R.P. Gangloff: in *Hydrogen Effects on Materials*, B.P. Somerday, P. Sofronis, and R.H. Jones, eds., ASM International, Materials Park, OH, 2009, pp. 1–21.
44. W.W. Gerberich, R.A. Oriani, M.-J. Lii, X. Chen, and T. Foecke: *Philos. Mag. A*, 1991, vol. 62, pp. 363–76.
45. R.P. Gangloff: in *Hydrogen Effects on Material Behavior and Corrosion Deformation Interactions*, N.R. Moody, A.W. Thompson, R.E. Ricker, G.S. Was, and R.H. Jones, eds., The Minerals, Metals & Materials Society, Warrendale, PA, 2003, pp. 477–97.
46. M.M. Hall, Jr. and D.M. Symons: in *Chemistry and Electrochemistry of Stress Corrosion Cracking*, R.H. Jones, ed., The Minerals, Metals & Materials Society, Warrendale, PA, 2001, pp. 447–66.
47. U. Komaragiri, S.R. Agnew, R.P. Gangloff, and M.R. Begley: *J. Mech. Phys. Solids*, 2008, vol. 56, pp. 3527–40.
48. C.D.S. Tuck, Z. Xianghua, and D.E.J. Talbot: *Br. Corros. J.*, 1994, vol. 29, pp. 70–74.
49. K.A. Nibur, B.P. Somerday, C. San Marchi, J.W. Foulk III, M. Dadfarnia, and P. Sofronis: *Metall. Mater. Trans. A*, 2013, vol. 44A, pp. 248–69.
50. J.P. Hirth: *Metall. Trans. A*, 1980, vol. 11A, pp. 861–90.
51. T.-Y. Zhang and J.E. Hack: *Metall. Mater. Trans. A*, 1999, vol. 30A, pp. 155–59.
52. M. Dadfarnia, P. Sofronis, B.P. Somerday, D.K. Balch, P. Schembri, and R. Melcher: *Eng. Fract. Mech.*, 2011, vol. 78, pp. 2429–38.
53. A. Taha and P. Sofronis: *Eng. Fract. Mech.*, 2001, vol. 68, pp. 803–37.
54. B.A. Kehler and J.R. Scully: *Corrosion*, 2008, vol. 64, pp. 465–77.
55. J. Waldman, R.P. Gangloff, and W.E. Garrison: Final Report, STTR Topic No. N08-T010 (Phase II), Navmar Applied Sciences Corporation, Warminster, PA, 2011.
56. R.A. Mayville, R.J. Warren, and P.D. Hilton: *Trans. ASME*, 1987, vol. 109, pp. 188–93.
57. J. Alvarez and F. Gutierrez-Solana: *Nucl. Eng. Des.*, 1999, vol. 188, pp. 185–202.
58. W. Dietzel, A. Atrens, and A. Barnoush: in *Gaseous Hydrogen Embrittlement of Materials in Energy Technologies*, R.P. Gangloff and B.P. Somerday, eds., Woodhead, Cambridge, 2012, vol. 1, pp. 237–73.
59. G.K. Dey and P. Mukhopadhyay: *Mater. Sci. Eng.*, 1986, vol. 84, pp. 177–89.
60. T.L. Anderson: *Fracture Mechanics*, 3rd edn, Taylor & Francis, Boca Raton, LA, 2005, pp. 121–23, 398–400, 445–46.
61. R.P. Gangloff, D.C. Slavik, R.S. Piascik and R.H. Van Stone: in *Small Crack Test Methods, ASTM STP 1149*, J.M. Larsen and J.E. Allison, eds., ASTM International, West Conshohocken, PA, 1992, pp. 116–68.

62. J.K. Donald and J. Ruschau: *Fatigue Crack Measurement: Techniques and Applications*, EMAS, West Midlands, 1991, pp. 11–38.
63. H.H. Johnson: *Mater. Res. Stand.*, 1965, vol. 5, pp. 442–45.
64. H. Tada, P.C. Paris, and G.R. Irwin: *The Stress Analysis of Cracks Handbook*, Paris Productions Incorporated, St. Louis, MO, 1985, pp. 2.10–2.12.
65. V. Kumar, M.D. German, and C.F. Shih: EPRI Final Report NP-1931, Electric Power Research Institute, Palo Alto, CA, 1981.
66. S.A. English and N.K. Arakere: *Int. J. Plast.*, 2011, vol. 27, pp. 920–39.
67. S. Cravero and C. Ruggieri: *Eng. Fract. Mech.*, 2007, vol. 74, pp. 2735–57.
68. A. Turnbull and J.G.N. Thomas: *J. Electrochem. Soc.*, 1982, vol. 129, pp. 1412–22.
69. J.S. Lee, M.L. Reed, and R.G. Kelly: *J. Electrochem. Soc.*, 2004, vol. 151, pp. B423–B433.
70. Y. Xu and H.W. Pickering: *J. Electrochem. Soc.*, 1993, vol. 140, pp. 658–68.
71. A.W. Hassel, K. Fushimi, and M. Seo: *Electrochem. Commun.*, 1999, vol. 1, pp. 180–83.
72. R.P. Gangloff: *Department of Defense 2013 Corrosion Conference*, NACE International, Houston, TX, 2013.
73. R. Bayles: Private Communication, Naval Research Laboratory, Washington, DC, 2012.
74. C.E. Price and G.W. Henderson: *Fatigue Fract. Eng. Mater. Struct.*, 1988, vol. 11, pp. 493–500.
75. B.P. Somerday, L.M. Young, and R.P. Gangloff: *Fatigue Fract. Eng. Mater. Struct.*, 2000, vol. 23, pp. 39–58.
76. R.A. Ainsworth: *Eng. Fract. Mech.*, 1984, vol. 19, pp. 633–42.
77. K.I. Azzabi, A.R. Luxmoore, and M.M.K. Lee: *Int. J. Fract.*, 1991, vol. 63, pp. 75–87.
78. X.-K. Zhu and J.A. Joyce: *Eng. Fract. Mech.*, 2012, vol. 85, pp. 1–46.
79. C.F. Shih and M.D. German: *Int. J. Fract.*, 1981, vol. 17, pp. 27–43.
80. C.F. Shih: *Int. J. Fract.*, 1985, vol. 29, pp. 73–84.
81. G.Y. Katz, N. Tymiak, and W.W. Gerberich: *Eng. Fract. Mech.*, 2001, vol. 68, pp. 619–46.
82. W.W. Gerberich, P.G. Marsh, and J.W. Hoehn: in *Hydrogen Effects in Materials*, A.W. Thompson and N.R. Moody, eds., TMS-AIME, Warrendale, PA, 1996, pp. 539–53.
83. R.A. Oriani: *Berichte Bunsen Gesellschaft fur Physik Chemistry*, 1972, vol. 76, pp. 848–57.
84. R.A. Oriani and P.H. Josephic: *Acta Metall.*, 1974, vol. 22, pp. 1065–74.
85. R.A. Oriani: *Corrosion*, 1987, vol. 43, pp. 390–97.
86. J.R. Rice and R. Thomson: *Philos. Mag.*, 1974, vol. 29, pp. 73–97.
87. M.R. Begley, J.A. Begley, and C.M. Landis: in *Gaseous Hydrogen Embrittlement of Materials in Energy Technologies*, R.P. Gangloff and B.P. Somerday, eds., Woodhead, Cambridge, vol. 1, 2012, pp. 286–325.
88. A. Nagao, C.D. Smith, M. Dadfarnia, P. Sofronis, and I.M. Robertson: *Acta Mater.*, 2012, vol. 60, pp. 5182–89.
89. M.L. Martin, I.M. Robertson, and P. Sofronis: *Acta Mater.*, 2011, vol. 59, pp. 3680–87.
90. S. Wang, M.L. Martin, P. Sofronis, S. Ohnuki, N. Hashimoto, and I.M. Robertson: *Acta Mater.*, 2014, vol. 69, pp. 275–82.
91. J.R. Scully and P.J. Moran: *J. Electrochem. Soc.*, 1988, vol. 135, pp. 1337–48.
92. C.J. McMahon, Jr: *Eng. Fract. Mech.*, 2001, vol. 68, pp. 773–88.
93. Y. Takeda and C.J. McMahon, Jr: *Metall. Trans. A*, 1981, vol. 12A, pp. 1255–66.
94. I.M. Robertson, M.L. Martin, and J.A. Fenske: in *Gaseous Hydrogen Embrittlement of Materials in Energy Technologies*, R.P. Gangloff and B.P. Somerday, eds., Woodhead, Cambridge, 2012, vol. 1, pp. 166–206.
95. D. Delafosse: in *Gaseous Hydrogen Embrittlement of Materials in Energy Technologies*, R.P. Gangloff and B.P. Somerday, eds., Woodhead, Cambridge, 2012, vol. 1, pp. 247–85.
96. J.E. Angelo, N.R. Moody, and M.I. Baskes: *Model. Simul. Mater. Sci. Eng.*, 1997, vol. 5, pp. 651–52.
97. D.M. Symons, G.A. Young, and J.R. Scully: *Metall. Mater. Trans. A*, 2001, vol. 32A, pp. 369–77.
98. Y. Shen and P.G. Shewmon: *Metall. Trans. A*, 1991, vol. 22A, pp. 1857–64.
99. P.G. Shewmon, Y.L. Shen, C.H. Shen, and M. Meshii: *Acta Metall.*, 1989, vol. 37, pp. 1913–21.
100. N.R. Moody, R.E. Stoltz, and M.W. Perra: *Metall. Trans. A*, 1987, vol. 18A, pp. 1469–82.
101. R.O. Ritchie and A.W. Thompson: *Metall. Trans. A*, 1985, vol. 16A, pp. 233–48.
102. http://www.specialmetals.com/products/monelalloyk500.php.